Suzaku View of the *Swift*/BAT Active Galactic Nuclei

by

Satoshi Eguchi

A dissertation submitted to Kyoto University in conformity with the requirements for the degree of Doctor of Philosophy.

Kyoto, Japan

January, 2011

Abstract

The cosmic X-ray background infer the existence of a significant fraction of Compton thick active galactic nuclei (AGNs), whose line-of-sight hydrogen column densities are greater than $\log N_{\rm H} \gtrsim 24$ cm^{-2}. Due to their strong photo-electric absorption, most of them can be missed in the previous surveys performed below 10 keV, and their nature is still unknown. Since the numerical studies suggest that most galaxies experience heavily obscured phase in their early stage, it is very important to obtain the high quality broad band spectra of buried AGNs, and to determine the geometrical structures such as the obscuring tori.

In the first half of this Ph.D. thesis, I present a systematic spectral analysis with *Suzaku* of six AGNs detected in the *Swift*/BAT hard X-ray (15–200 keV) survey, Swift J0138.6–4001, J0255.2–0011, J0350.1–5019, J0505.7–2348, J0601.9–8636, and J1628.1–5145. This is considered to be a representative sample of new AGNs without X-ray spectral information before the BAT survey. I find that the 0.5–200 keV spectra of these sources can be uniformly fit with a base model consisting of heavily absorbed ($\log N_{\rm H}$ >23.5 cm^{-2}) transmitted components, scattered lights, a reflection component, and an iron-K emission line. There are two distinct groups, three "new type" AGNs (including the two sources reported by Ueda et al. 2007) with an extremely small scattered fraction ($f_{\rm scat} < 0.5\%$) and strong reflection component ($R = \Omega/2\pi \gtrsim 0.8$ where Ω is the solid angle of the reflector), and three "classical type" ones with $f_{\rm scat} > 0.5\%$ and $R \lesssim 0.8$. The spectral parameters suggest that the new type has an optically thick torus for Thomson scattering ($N_{\rm H} \sim 10^{25}$ cm^{-2}) with a small opening angle $\theta_{\rm oa} \sim 20^\circ$ viewed in a rather face-on geometry, while the

classical type has a thin torus ($N_{\rm H} \sim 10^{23-24}$ cm^{-2}) with $\theta_{\rm oa} \gtrsim 30^{\circ}$. I infer that a significant number of new type AGNs with an edge-on view is missing in the current all-sky hard X-ray surveys.

In the last half of this thesis, I report the broad band spectra of two *Swift*/BAT AGNs (NGC 612 and NGC 3081) obtained from *Suzaku* follow-up observations and the results of the spectral analyses with a new method. Fitting with standard models, I find that both sources show similar spectra characterized by a heavy absorption with $N_{\rm H} \simeq 10^{24}$ cm^{-2}, the fraction of scattered light is $f_{\rm scat} = 0.5 - 0.8\%$, and the solid angle of the reflection component is $\Omega/2\pi = 0.4 - 1.1$. To investigate the geometry of the torus, I apply numerical spectral models utilizing Monte Carlo simulations by Ikeda et al. (2009) to the *Suzaku* spectra. I find my data are well explained by this torus model, which has only four geometrical parameters. The fit results suggest that NGC 612 has the torus half opening-angle of $\simeq 60^{\circ} - 70^{\circ}$ and is observed from a nearly edge-on angle with a small amount of scattering gas, while NGC 3081 has a very small opening angle $\simeq 15^{\circ}$ and is observed on a face-on geometry, more like the deeply buried "new type" AGNs found by Ueda et al. (2007). I demonstrate the potential power of direct application of such numerical simulations to the high quality broad band spectra to unveil the inner structure of AGNs.

Acknowledgements

I sincerely appreciate all people I met in the past five years. This thesis is a summarization of my wonderful interaction with them. Firstly, I have to thank my boss, Dr. Ueda. He taught me an ABC for the way how to conduct a reseach as well as the X-ray astronomy. His lessons gave me an inspiration for the application of the Ikeda torus model. Though I owed a lot to him in the process of boiling down the discussion, I believe that I became an independent researcher. Secondly, I appreciate Dr. Mineshige and Dr. Masada; they gave me a lot of valuable advice when I lost my direction in life. I could be a dropout if they were not. Lastly, I have to apologize to the people struggling with *MAXI* for the unnessesary frictions and my retire. There was no choise to keep up my mental stability. I will make it up to them indirectly by drawing on my precious experience of *MAXI* for the future *DECIGO* mission.

Contents

List of Figures

List of Tables

Chapter 1

General Introduction

1.1 Active Galactic Nuclei and the Unified Model

An active galactic nucleus (AGN) is a galaxy which emits huge amount of energy in wide energy bands. It consists of a supermassive black hole (SMBH) with the mass of $10^{6-9} M_{\odot}$, an accretion disk as the energy source, and dust torus (Figure 1.1). They are roughly classified into two groups whether they have a set of broad emission lines ($\sim (1-5) \times 10^3$ km s^{-1}) of H I, He I, and He II, or not; the one with broad emission lines is called Type 1, and the other is called Type 2. Narrow emission lines of [O III]$\lambda\lambda 4959, 5007$, [N II]$\lambda\lambda 6548, 6583$, and [S II]$\lambda\lambda 6716, 6731$ are commonly observed for both types.

Antonucci & Miller (1985) detected a polarized broad emission line which was as broad as the broad lines seen in Type 1 galaxies in the spectrum of NGC 1068, a Type 2 galaxy. The polarization was interpreted as the result of scattering of light by dust or electrons into our line of sight. Hence they confirmed that a dust torus surrounds the nucleus, and that the difference between Type 1 and Type 2 is caused by the viewing angle of the torus. This is well known as the unified model of AGNs; the region emitting the broad lines (broad line region; BLR) locates inside of the torus and have wide velosity dispersion due to the strong gravity of the SMBH, and the region emitting the narrow lines (narrow line region; NLR) locates outside of the torus. Since the BLR is hidden by the torus, no broad emission line is detected and

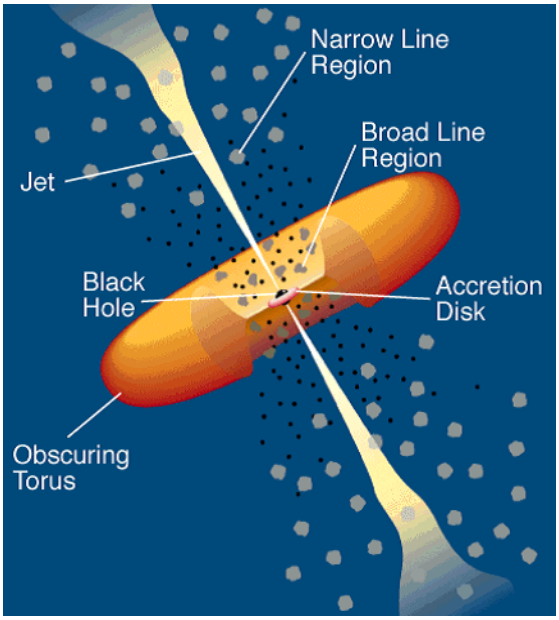

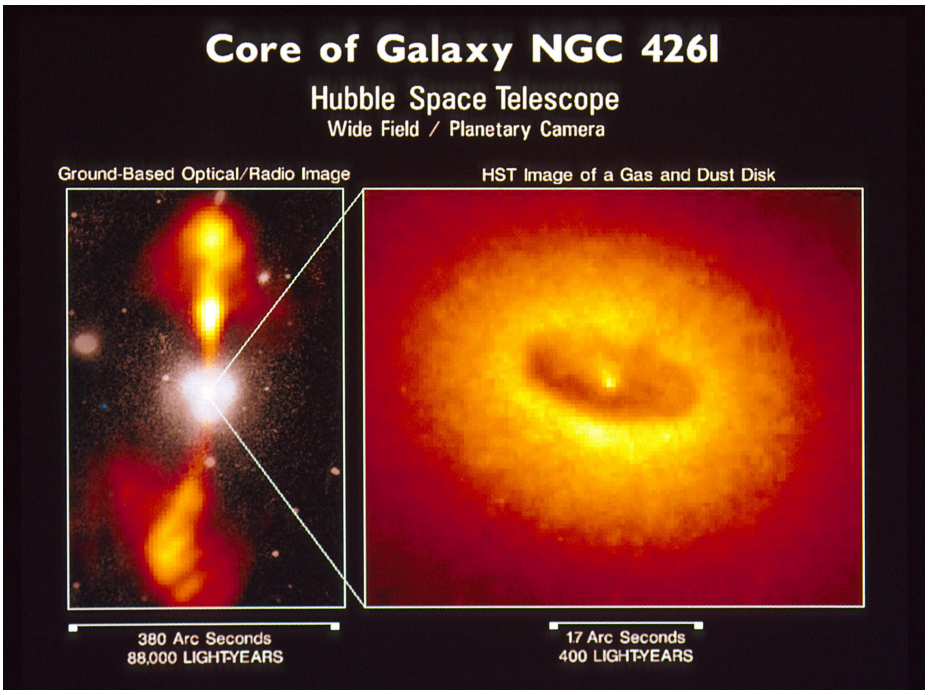

Figure 1.1 The cartoon of an AGN by Urry & Padovani (1995) (top) and the central region of NGC 4261 (bottom) observed with the *Hubble Space Telescope* (bottom). A torus is often illustrated in a doughnut-like shape in the unified model of AGNs, however, its structure is still under debate.

the object is recognized as Type 2 if we are seeing it from an edge-on angle. A torus is often illusrated as a doughnut in the unified model of AGNs like the top panel in Figure 1.1. Though the geometry of a torus is still under debate, doughnut-like tori account for many observations qualitatively.

1.2 The Cosmic X-ray Background and Compton Thick AGNs

The cosmic X-ray background (CXB) is the diffuse emission with an approximately constant intensity from all directions. It was discovered with the rocket flight performed by Giacconi et al. (1962) in order to detect the X-ray emission from the Moon. The development of Wolter telescopes enabled us sensitive and high-angular-resolution X-ray observations, and revealed that the origin of CXB is the ensemble emission from a number of AGNs. For instance, deep surveys with *ROSAT* in the 0.5–2 keV band at fluxes down to $\approx 10^{-15}$ ergs cm^{-2} s^{-1} resolved $\approx 75\%$ soft CXB into discrete sources (e.g., Hasinger et al. 1993, 1998), and subsidiary extensive follow-up observations in the optical wavelength identified them as AGN (e.g., McHardy et al. 1998). The recent *Chandra* deep servey resolved $\sim 80\%$ of CXB in the 0.5–8 keV band into discrete sources (Hickox & Markevitch 2006). It is now widely believed that whole CXB spectrum below ~ 100 keV can be accounted for by the emissions from both of unobscured and obscured AGNs integrated over the cosmic history.

On the other hand, the further studies concering CXB raised an fundamental question about the population of AGNs. Figure 1.2 represents the observed CXB spectrum with various X-ray observatories and the estimated contributions from unobscured ($\log N_{\rm H}$ (cm^{-2}) $\lesssim 21.5$), Compton thin ($21.5 \lesssim \log N_{\rm H} \lesssim 23.5$), Compton thick AGNs ($\log N_{\rm H} \gtrsim 24.5$), and their total, respectively. The ensemble spectra of both unobscured and Compton thin AGNs are obtained directly by the individual observations. This figure shows that there must be a significant number of Compton thick AGNs, which it is difficult to detect directly due to strong photo-electric absorption below 10 keV, are required to account for the peak of the CXB spectrum around

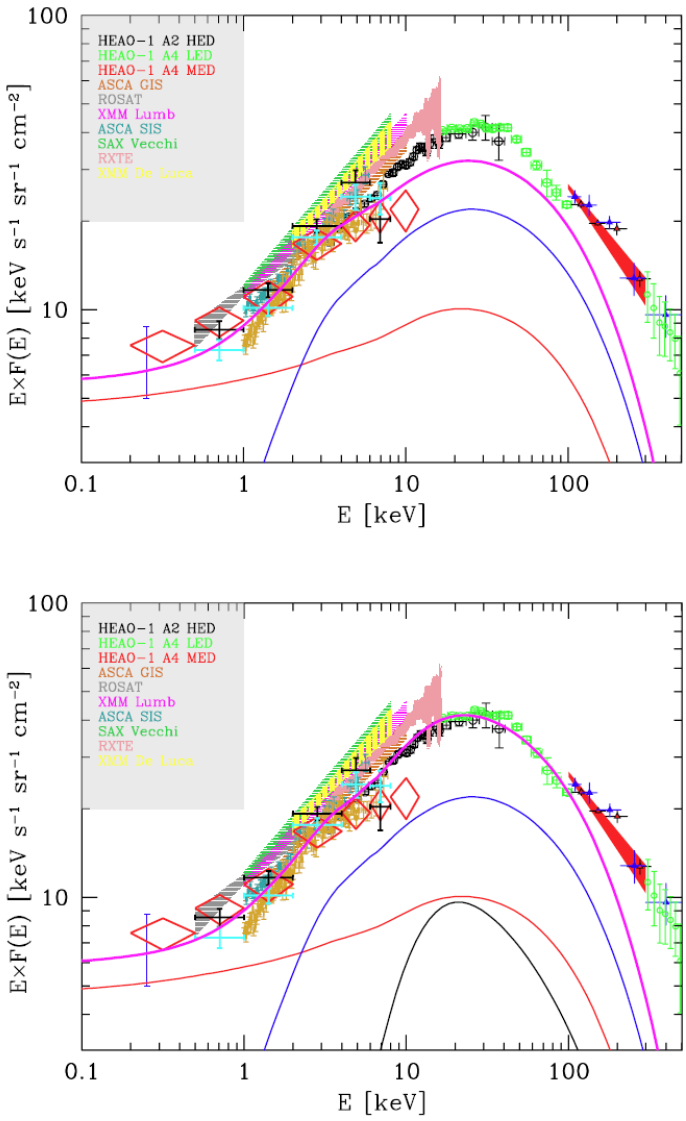

Figure 1.2 The contributions of emissions from AGNs with the different line-of-sight hyderogen column densities ($N_{\rm H}$ in the units of cm^{-2}) to CXB by Gilli et al. (2007). The crosses and diamonds represent the observed spectum of CXB with various satellites, while the red, blue, black, and magenta lines correspond to the estimated emissions from unobscured ($\log N_{\rm H} \lesssim 21.5$), Compton thin ($21.5 \lesssim \log N_{\rm H} \lesssim 23.5$), Compton thick ($\log N_{\rm H} \gtrsim 24.5$) AGNs, and the total of them, respectively. There remain significant residuals around 30 keV if the contribution from the Compton thick AGNs are not considered (top), while the observed CXB spectrum below 100 keV are reproduced well if it is taken into account (bottom).

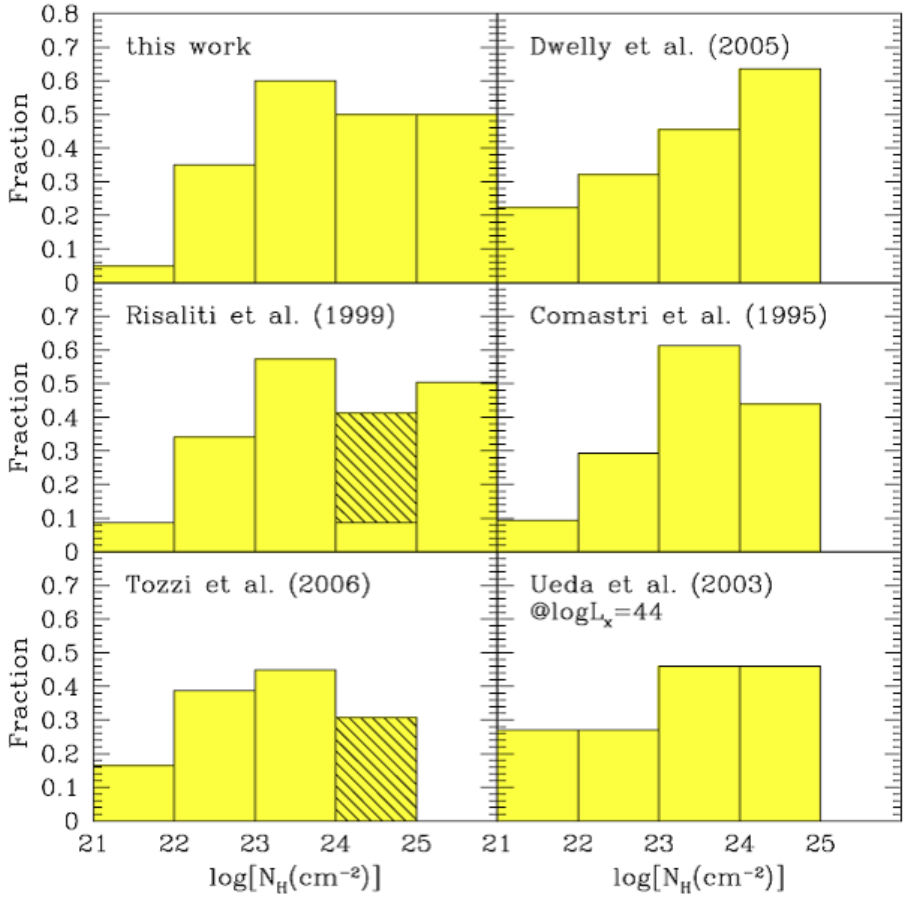

Figure 1.3 The $N_{\rm H}$ distributions estimated from the CXB spectrum by Gilli et al. (2007). The number of objects in each $N_{\rm H}$ bin is normalized to the total number of Compton thin ($21 < \log N_{\rm H} < 24$) AGN. This suggests that there are a large number of Compton thick ($\log N_{\rm H} \gtrsim 24$) in universe.

30 keV. In other words, the residuals from the CXB spectrum correspond to the canonical spectrum of Compton thick AGNs, which are not resolved individually yet. The fraction of Compton thick AGNs to Compton thin ones is studied and discussed extensively (e.g., Ueda et al. 2003; Gilli et al. 2007), and found to be very major in universe (Figure 1.3). Note that the fraction tightly depends on the spectral shape of a "standard" Compton thick AGN. The distinct Compton reflection component from a torus ($R \equiv \Omega/2\pi \sim 1$, where Ω is the solid angle of the reflector) is approximated by the **pexrav** model (Magdziarz & Zdziarski 1995) in *XSPEC*, which intends to represent the Compton reflection from an accretion disk, in much literature. Since the shape of the Compton reflection strongly depends on the geometry of a reflector, it is very essential for unified understanding of AGNs including Compton thick ones to obtain the "real" spectra of Compton thick AGNs and to constrain their geometries.

1.3 Compton Thick AGNs and the Galaxy Evolutions

It is well known that there is a strong correlation between the mass of a SMBH and that of the galactic bulge (Figure 1.4; Magorrian relation; Magorrian et al. e.g., 1998; Marconi & Hunt e.g., 2003). This suggests a fundamental link between the growth of SMBH and galaxy evolution. In fact, the theoretical study performed by Hopkins et al. (2005) demonstrates that a SMBH experiences a heavily obscured ($\log N_{\rm H} \gtrsim 24$ cm^{-2}, i.e., Comton thick) phase in its growth stage (Figure 1.5). Star formation, supernova and AGN feedback are taken into accout in their simulations. Here I mention the case of $V_{\rm vir} = 226$ km s^{-1}, $M_{\rm vir} = 3.8\times10^{12}\odot$, and $M_{\rm BH} = 7\times10^{8}\odot$, where $V_{\rm vir}$ is the initial virial verocity, $M_{\rm vir}$ is the initial virial mass, and $M_{\rm BH}$ is the final SMBH mass, respectively. Once the merger begins, the gas concentrates on the center of the system, and the intrinsic luminosity rapidly rises at ~ 1.6 Gyr from the start of the simulation. However, the galaxy cannot be observed becase of the very large column density at the time. After a short time (~ 0.1 Gyr), the AGN feedback disperses the gas in the center of the system, and the galaxy can be seen as a AGN.

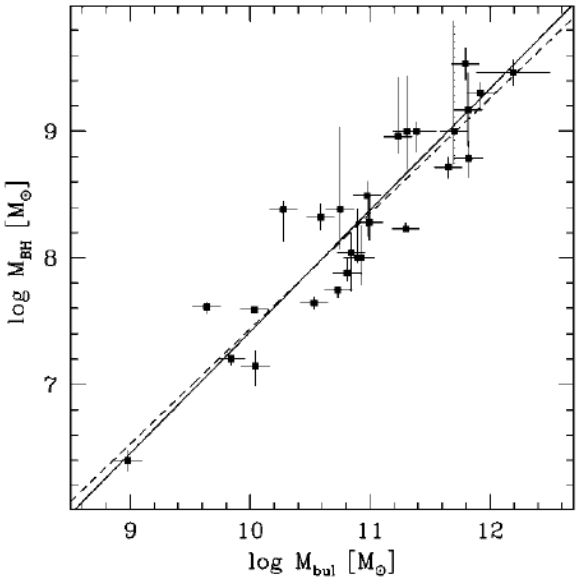

Figure 1.4 The correlation between the mass of a SMBH and that of the galactic buldge known as Magorrian relation by Marconi & Hunt (2003).

A rapid accretion onto the SMBH takes place in this stage.

In the context of hierarchical structure formations, the merging of galaxies has happened many times in the past, thus they also propose a "cosmic cycle" for galaxy formation and evolution (Figure 1.6). From theorerical aspects as well as the CXB spectrum, there are believed that a large fraction of heavily obscured or Compton thick objects can be missed from previous surveys in the optical wavelengths.

1.4 The Aims of This Ph.D. Thesis

Recent X-ray and IR observations have revealed populations of AGNs without any signature of AGNs in the optical band (e.g., Maiolino et al. 2003). This fact implies that AGN surveys relying on optical emission signatures (such as the [O III] λ5007 line) may be incomplete.

Sensitive hard X-ray observations above 10 keV provide us with the least biased AGN samples in the local universe, due to the strong penetrating power against photo-electric absorption, except for heavily Compton thick (column density of $\log N_{\rm H} \gtrsim$

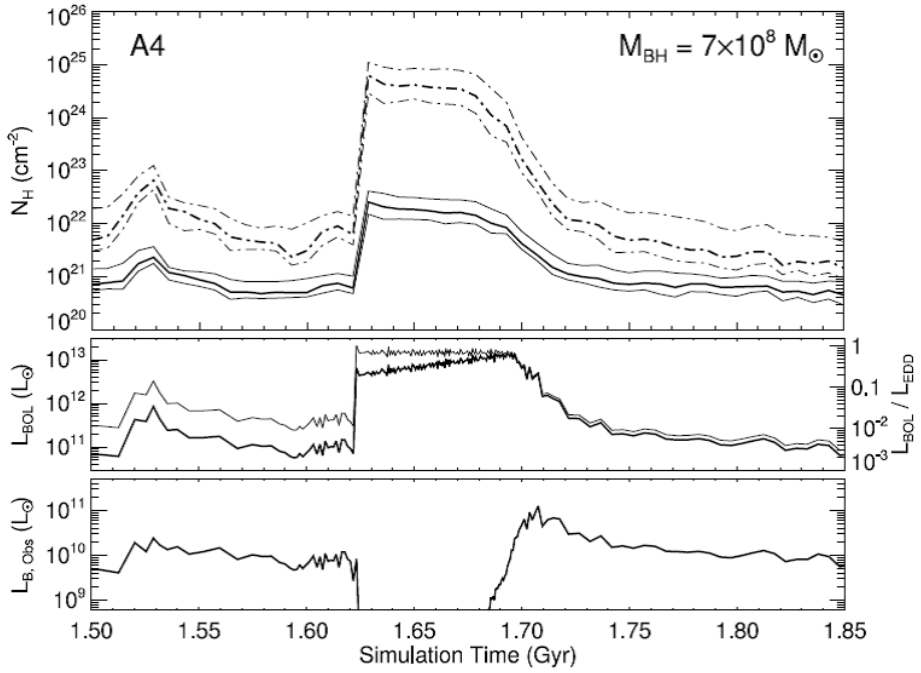

Figure 1.5 The median column density as a function of simulation time by Hopkins et al. (2005). The merging process of two equal-mass galaxies are traced; the initial virial velocities, the masses of galaxies, and final one of the SMBH are set to be 226 km s^{-1}, $3.8 \times 10^{12}\odot$, and $7 \times 10^{8}\odot$, respectively. The thick solid, dashed line represent the median column density ($N_{\rm H}$) of the hot-phase interstellar medium and that of the total with the contours at 25% and 75% inclusion levels. The bolometric (left middle) and observed B-band (left bottom) luminosities are also presented. In the simulation, the AGN feedback is taken into account.

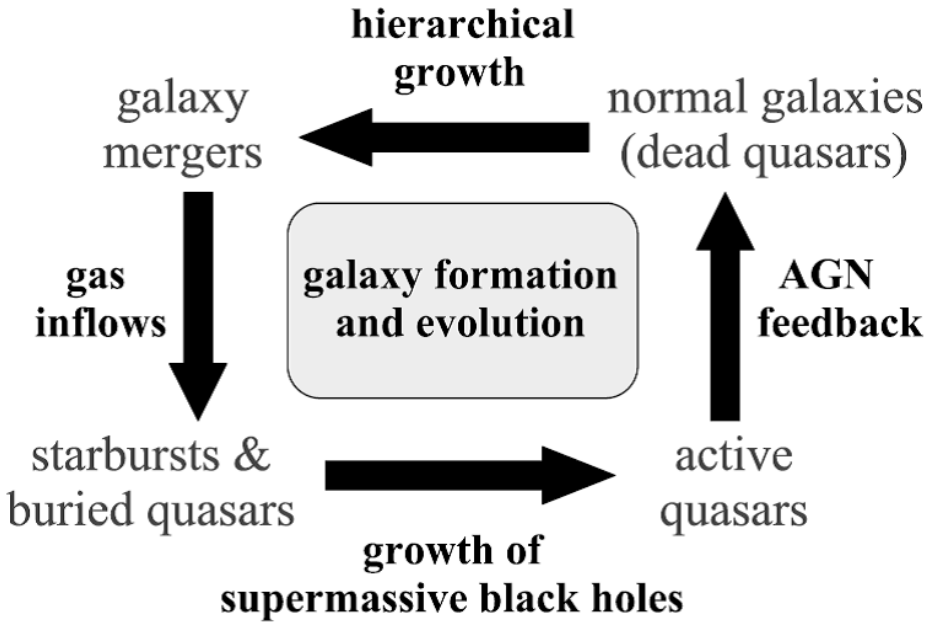

Figure 1.6 The schematic diagram of galaxy evolution by Hopkins et al. (2006). Based on the simulation results by Hopkins et al. (2005), the autors propose "buried quasar" phase into a cosmic cycle for galaxy formation and evolution.

24.5 cm^{-2}) objects. Recent all sky hard X-ray surveys performed with *Swift*/BAT (Tueller et al. 2008) and *INTEGRAL* (Bassani et al. 2006; Krivonos et al. 2007) have started to detect many local AGNs with about 10 times better sensitivity than that of previous missions in this energy band. They have shown that roughly half of all local AGN are indeed obscured AGNs. These hard X-ray samples contain a number of new AGNs, for which detailed follow-up studies have not been done yet. Some of these sources objects were not recognized to be AGNs previously even though there were optical imaging and spectroscopy data available.

Our team has started to make follow-up observations of selected *Swift*/BAT AGNs with the *Suzaku* satellite to obtain the best quality broad band high energy data. The major purposes are (1) to discover new populations of AGNs, (2) to measure their spectral properties, which make it possible to construct the $N_{\rm H}$ distribution of a complete *Swift*/BAT sample, and (3) to accurately constrain the strength of the reflection component, which is an important yet uncertain parameter in population synthesis models of the CXB in explaining its broad-band shape (Ueda et al. 2003; Gilli et al. 2007). In particular, the simultaneous coverage over the 0.2–70 keV band with *Suzaku* is crucial to discriminate degeneracy of spectral models under possible time variability and to determine the amounts of scattered and reflected components, key information to constrain the geometry of surrounding matter around the nucleus.

Most previous studies, however, relied on phenomenological spectral models where the detailed geometry of the torus is not taken into account; usually, an analytical formula for the Compton reflection from matter with infinite optical depths is simply assumed for the reprocessed emission, and absorption column density of the transmitted component is treated independently. Monte Carlo simulation is a powerful tool to reproduce realistic spectra from AGNs with a complex structure of the torus, which may not always have a sufficiently large optical depth for Compton scattering. Recently, Ikeda et al. (2009) have developed such a Monte Carlo code that can be applicable to the broad band X-ray spectra with several free parameters describing the torus geometry. Similarly, Murphy & Yaqoob (2009) also studied the numerical

spectra from a toroidal torus, known as the MYTORUS model[1], although I do not adopt this model here because the opening angle of the torus is fixed at 60°. Applying such models directly to the observed spectra, we can obtain more accurate constraints on the inner structure of AGNs than from the standard previous analysis.

The first results obtained from the *Suzaku* follow-up of two *Swift*/BAT AGNs led to the discovery of a new type of deeply buried AGNs that exhibit very small fractions of scattered soft X-rays ($< 0.5\%$) with respect to the transmitted component, with strong reflection signals most probably coming from the inner wall of the Compton-thick tori (Ueda et al. 2007). In Chaper 2 of this Ph.D. thesis, I present the results of a detailed analysis of six *Swift*/BAT AGNs, including the two sources (Swift J0138.6–4001 and Swift J0601.9–8636) already reported there[2] with standard analytical models, and then show that they could be classified into two types, "new type" AGNs with a small scattering fraction and strong reflection strength, and "classical type" ones with a larger scattering fraction and weaker reflection.

In Chaper 3, I present the results of detailed X-ray spectral analysis of *Suzaku* data of two *Swift*/BAT AGNs, Swift J0134.1–3625 (NGC 612; $z = 0.0298$) and Swift J0959.5–2258 (NGC 3081; $z = 0.0080$), whose simultaneous broad band spectra were not available before. I first analyze the spectra with standard spectral models, and then present the results of application of the torus model utilizing Monte Carlo calculation by Ikeda et al. (2009). I adopt the cosmological parameters $(H_0, \Omega_{\rm m}, \Omega_\lambda) = (70 \text{ km s}^{-1} \text{ Mpc}^{-1}, 0.3, 0.7)$ throughout the paper.

[1] `http://www.mytorus.com/`

[2] For these two sources, the results of the present paper, which are based on more recent calibration of the instruments and background estimation, supersedes those by Ueda et al. (2007), although the essence is not changed.

Chapter 2

Spectral Analysis of Six AGNs and Evidence for Two Types of Obscured Population

2.1 Introduction

The first results obtained from the *Suzaku* follow-up of two *Swift*/BAT AGNs led to the discovery of a new type of deeply buried AGNs (Ueda et al. 2007). Here I present the results of a detailed analysis of six *Swift*/BAT AGNs, including the two sources (Swift J0138.6–4001 and Swift J0601.9–8636) already reported there. Section 2.2 summarizes the sample and observations. In Section 2.3, I mainly present the results of detailed spectral analysis with *Suzaku*. Discussion is given in Section 2.4.

2.2 Observations

I observed six *Swift*/BAT AGNs with *Suzaku* between 2006 April and 2007 January in the AO-1 phase. The targets are Swift J0138.6–4001, J0255.2–0011, J0350.1–5019, J0505.7–2348, J0601.9–8636, and J1628.1–5145, whose identification in the optical or infrared band is ESO 297–G018, NGC 1142, 2MASX J03502377–5018354, 2MASX J05054575–2351139, ESO 005–G004, and Mrk 1498, respectively (Tueller et al. 2008).

Table 2.1. List of Targets

SWIFT	Optical/IR Identification	R.A. (J2000)	Dec. (J2000)	Redshift	Classification
J0138.6–4001	ESO 297–G018	01 38 37.16	-40 00 41.1	0.0252	Seyfert 2
J0255.2–0011	NGC 1142	02 55 12.196	-00 11 0.81	0.0288	Seyfert 2
J0350.1–5019	2MASX J03502377–5018354	03 50 23.77	-50 18 35.7	0.036	Galaxy
J0505.7–2348	2MASX J05054575–2351139	05 05 45.73	-23 51 14.0	0.0350	Seyfert 2
J0601.9–8636	ESO 005–G004	06 05 41.63	-86 37 54.7	0.0062	Galaxy
J1628.1+5145	Mrk 1498	16 28 4.06	+51 46 31.4	0.0547	Seyfert 1.9

Note. — The position, redshift, and classification for each source is taken from the NASA/IPAC Extragalactic Database.

The basic information of my targets is summarized in Table 2.1. 2MASX J03502377–5018354 and ESO 005–G004 had not been identified as active galaxies in the optical band, and revealed to contain an AGN for the first time with the detection of hard X-rays by the BAT. The sources were selected as the *Suzaku* targets because at the time of my proposals these "new" *Swift* AGNs had no spectral information available below 10 keV. Recently short follow-up observations of these targets have been carried out with *XMM-Newton* or the X-Ray Telescope (XRT) onboard *Swift* (Winter et al. 2008).

Suzaku, the fifth Japanese X-ray satellite (Mitsuda et al. 2007), carries four X-ray CCD cameras called the X-ray Imaging Spectrometer (XIS-0, XIS-1, XIS-2, and XIS-3; Koyama et al. 2007) as focal plane imager of four X-ray telescopes, and a non-imaging instrument called the Hard X-ray Detector (HXD; Takahashi et al. 2007) consisting of Si PIN photo-diodes and GSO scintillation counters. XIS-0, XIS-2, and XIS-3 are front-side illuminated CCDs (FI-XISs), while XIS-1 is the back-side illuminated one (BI-XIS).

In this paper, I analyze the data of the XISs and the HXD/PIN (HXD nominal position), which covers the energy band of 0.2–12 keV and 10–60 keV, respectively, since the fluxes of my targets above 50 keV are too faint to be detected with the HXD/GSO. Table 2.2 shows the log of the observations. The net exposure of Swift

Table 2.2. Observation Log

SWIFT	Start Time (UT)	End Time	Exposure[a](XIS)	Exposure (HXD/PIN)	SCI[b]
J0138.6–4001	2006 Jun 04 18:13	Jun 05 05:00	21.2 ks	16.5 ks	Off
J0255.2–0011	2007 Jan 23 14:54	Jan 26 05:30	101.6 ks	80.6 ks	On
J0350.1–5019	2006 Nov 23 02:07	Nov 23 13:33	19.3 ks	15.7 ks	On
J0505.7–2348	2006 Apr 01 22:12	Apr 04 02:55	78.6 ks	50.3 ks	Off
J0601.9–8636	2006 Apr 13 16:24	Apr 14 01:52	19.8 ks	15.7 ks	Off
J1628.1+5145	2006 Apr 15 18:49	Apr 16 09:22	23.6 ks	19.5 ks	Off

[a]Based on the good time interval for XIS-0.

[b]With/without the spaced-row charge injection for the XIS(Nakajima et al. 2008).

J0255.2–0011 and Swift J0505.7–2348 is about 100 ks and 80 ks, respectively, while that for the rest 4 targets is 20 ks each[1]. Because XIS-2 became unoperatable on 2007 November 7 (Dotani et al. 2007), no XIS-2 data are available for Swift J0255.2–0011 and Swift J0350.1–5019. For the observations of Swift J0255.2–0011 and Swift J0350.1–5019, I applied spaced-row charge injection (SCI) for the XIS data to improve the energy resolution (Nakajima et al. 2008). In the spectral analysis, I also utilize the BAT spectra covering the 15–200 keV band, integrated for the first 9 months for Swift J0138.6–4001 and Swift J0601.9–8636, and for 22 months for the rest of targets.

2.3 Analysis and Results

I analyze the *Suzaku* data using *HEAsoft* version 6.3.2 from the data products version 2.0 distributed by the *Suzaku* pipeline processing team. In extraction of the light curves and spectra, I set the source region as a circle around the detected position with a radius of 1.5–2 arcmin, depending on the flux. For the XIS data, the background was taken from a source-free region in the field of view with an

[1]The primary goal of the first two targets is to constrain the reflection component with the best accuracy, aiming at the brightest new sources in the (then) latest BAT catalog. For the four targets with 20 ks exposure, the main goal was to obtain their X-ray spectra below 10 keV to make the BAT sample complete.

approximately same offset angle from the optical axis as the source. For the HXD/PIN data, I use the so-called "tuned" background model provided by the HXD team. Its systematic errors are estimated to be $\simeq 1.3\%$ at a 1σ confidence level in the 15–40 keV band for a 10 ks exposure (Mizuno et al. 2008). As my exposures are $\approx$20 ks or larger, I expect that the error is even smaller than this value.

2.3.1 Light Curves

Figures 2.1 and 2.2 show the background-subtract light curves of my targets obtained with the XIS and HXD in the 2–10 keV and 15–40 keV band, respectively. To minimize any systematic uncertainties caused by the orbital change of the satellite, I merge data taken during one orbit (96 minutes) into one bin. Then, to check if there is any significant time variability during the observations, I perform a simple χ^2 test to each light curve assuming a null hypothesis of a constant flux. The resultant reduced χ^2 value and the degree of freedom are shown in each panel. I detect no significant time variability on a time scale of hours for all the targets in both energy bands. Thus, I analyze the spectra of all the targets averaged over the whole observation epoch.

2.3.2 BAT Spectra

Before performing the spectral fit to the *Suzaku* data, I firstly analyze only the BAT spectra in the 15–200 keV band to constrain the high energy cutoff in the continuum. It is known that the incident photon spectra of Seyfert galaxies are well approximated by a power law with an exponential cutoff (cutoff power law model), represented as $AE^{-\Gamma}\exp\{-E/E_{\rm cut}\}$, where A, Γ, $E_{\rm cut}$ is the normalization at 1 keV, photon index, cutoff energy, respectively. Here I utilize the **pexrav** code by Magdziarz & Zdziarski (1995) to take into account possible contribution of the Compton reflection component from optically thick, cold matter. The relative intensity of the reflection component to that of the incident cutoff power law component is defined as $R \equiv \Omega/2\pi$, where Ω is the solid angle of the reflector ($R = 1$ corresponds to the reflection from a semi-infinite plane).

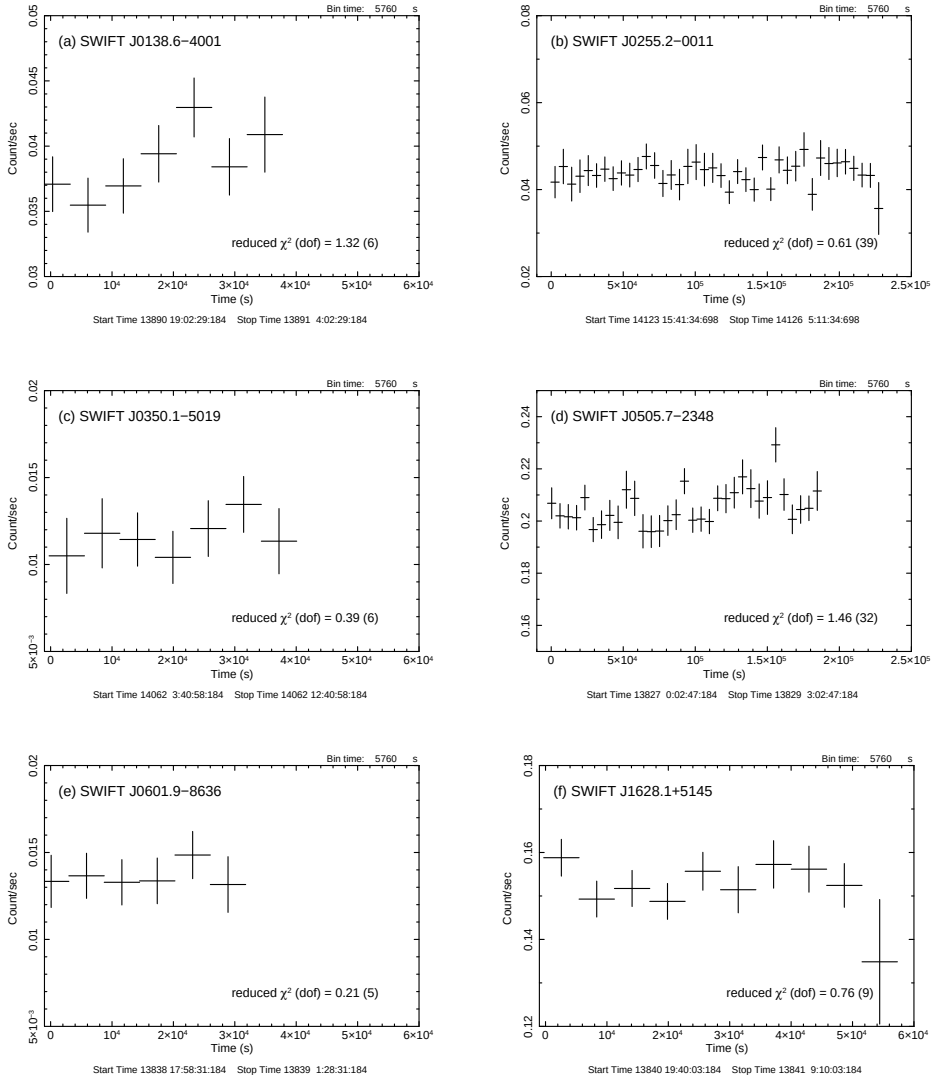

Figure 2.1 The background subtracted light curves of XIS in the 2–10 keV band during the *Suzaku* observations. One bin corresponds to 96 minutes. The data from the XIS-0 and XIS-2 are summed for Swift J0255.2–0011 and Swift J0350.1–5019, while those from XIS-0, XIS-2, and XIS-3 are summed for the rest. The numbers listed in each panel represent the value of reduced χ^2 with the degree of freedom for the constant flux hypothesis.

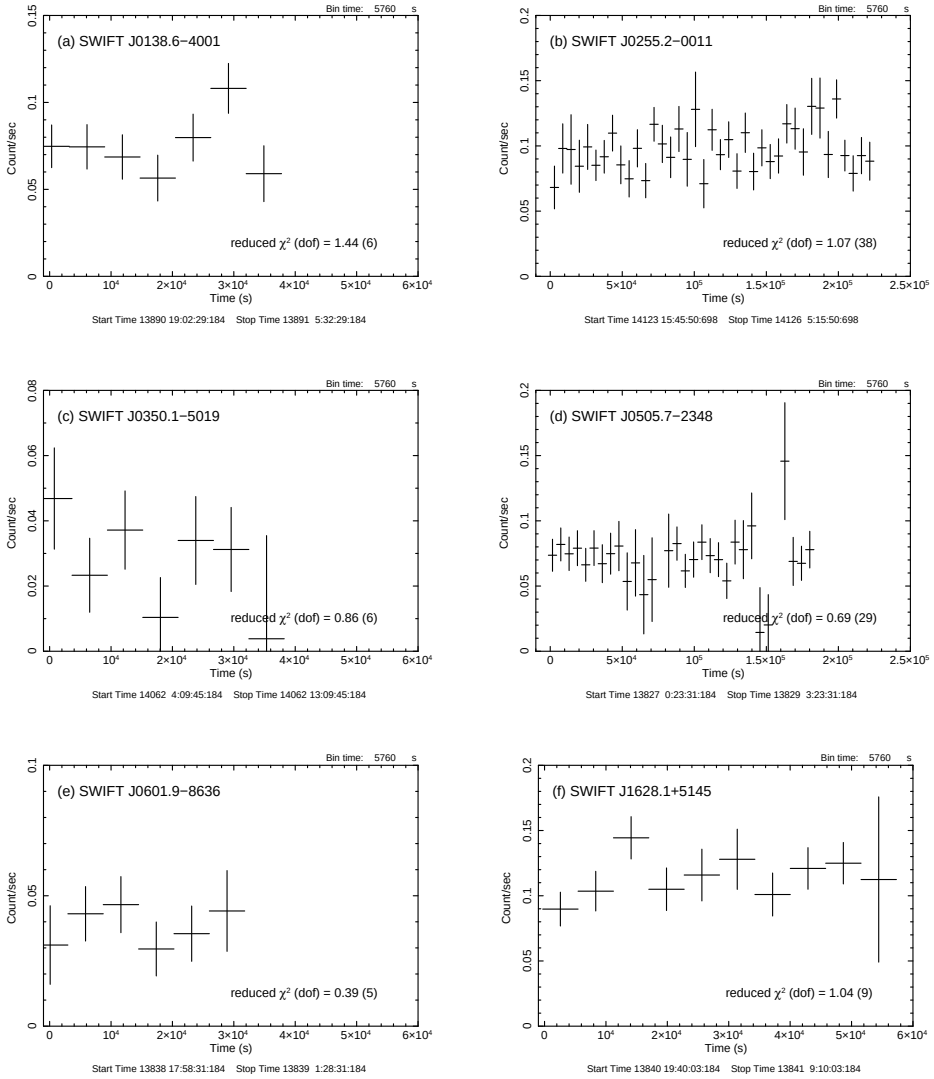

Figure 2.2 The background subtracted light curves of HXD/PIN in the 15–40 keV band during the *Suzaku* observations. One bin corresponds to 96 minutes. The numbers listed in each panel represent the value of reduced χ^2 with the degree of freedom for the constant flux hypothesis.

Table 2.3. Cutoff Energies ($E_{\rm cut}$) determined by the BAT spectra

$\Omega/2\pi$	SWIFT J0138.6–4001	J0255.2–0011	J0350.1–5019	J0505.7–2348	J0601.9–8636	J1628.1+5145
0	> 317	> 289	> 106	> 318	> 116	> 99
χ^2/d.o.f.	1.58/2	4.57/6	1.16/6	13.58/6	4.96/2	2.38/6
2	329 (> 91)	> 253	> 95	> 306	> 82	> 87
χ^2/d.o.f.	1.05/2	5.21/6	2.40/6	15.24/6	3.37/2	4.61/6

Note. — The unit of $E_{\rm cut}$ is keV.

In this stage, I assume $R = 0$ or 2 as the two extreme cases just to evaluate the effects of the reflection. The inclination angle is fixed at 60°. To avoid strong coupling between the power law slope and and cutoff energy, I fix the photon index at 1.9, which is a canonical value for AGNs. Table 2.3 summarizes the fitting results of the cutoff energy for each target. While it is difficult to constrain its upper limit due to the limited band coverage of the BAT, I find the cutoff energy must be above ≈100 keV in most cases. Considering this limitation, I fix $E_{\rm cut}$ at 300 keV in all subsequent analysis. Impacts by adopting a lower value of $E_{\rm cut}$ in the spectral fitting are discussed in §2.3.5.

2.3.3 Spectral Models

I consider three basic models in the spectral analysis uniformly for all the six targets. My policy is to start with the simplest model for each target; if I find that the fit with a simple model does not give a physically self-consistent picture and/or that the fit is significantly improved by introducing additional parameters, then I adopt more complicated models. In all the cases, I assume a power law with an exponential cutoff fixed at 300 keV for the incident continuum, as explained in the previous subsection. The Galactic absorption, $N_{\rm H}^{\rm Gal}$, is always included in the model (even if not explicitly mentioned below) by assuming the hydrogen column density from the H I map of Kalberla et al. (2005), available with the *nh* program

in the *HEAsoft* package. For absorption, I adopt the photo-electric absorption cross section by Balucinska-Church & McCammon (1992) ("bcmc") and use the **phabs** or **zphabs** model in XSPEC. Solar abundances by Anders & Grevesse (1989) are assumed throughout the analysis.

The first (simplest) model, designated as Model A, consists of (i) a transmitted component (a cut-off power law absorbed by cold matter), (ii) a scattered component (a cut-off power law without absorption), and (iii) an iron-K emission line (a gaussian), represented as **zphabs*zhighect*zpowerlw + const*zhighect*zpowerlw + zgauss** in the XSPEC terminology[2]. According to the unified scheme, in type 2 AGNs, the incident power law from the nucleus will be absorbed by a dusty torus around the SMBH, while the nuclear emission is partially scattered into the line-of-sight by ionized gas around the torus. For simplicity, I assume that the scattered component has the same shape of the incident power law with a fraction of $f_{\rm scat}$ as first-order approximation, although, in reality, it often contains a number of recombination lines produced by a photo-ionized plasma (e.g., Sako et al. 2000) unless the scatterer is fully ionized. As a result of reprocessing by cold matter in the surrounding environment (such as a torus, an ionized gas, and an accretion disk), an iron-K emission will be produced at the rest-frame 6.4 keV. Since a line from the torus should not resolved by the energy resolution of the XIS, I fix the 1σ line width of the iron-K line at the averaged value of the (apparent) line width of the ^{55}Fe calibration source at 5.9 keV: 0.3 eV, 38 eV, 30 eV, 0.8 eV, 1.7 eV and 3.2 eV for Swift J0138.6–4001, J0255.2–0011, J0350.1–5019, J0505.7–2348, J0601.9–8636, and J1628.1–5145, respectively, to take into account a possible systematic error in the energy response [3].

In the second model, Model B, I consider an additional contribution of an absorbed Compton reflection component from optically thick matter. This emission is expected from the inner wall of an (optically thick) torus and/or the accretion disk, irradiated by the incident continuum. Model B is expressed as **zphabs*zhighect*zpowerlw + const*zhighect*zpowerlw + zgauss + zphabs*pexrav** in the XSPEC ter-

[2]the **zhighect** model is utilized to represent exponential cutoff at the source redshift.

[3]The large line widths of Swift J0255.2–0011 and J0350.1–5019 are artifact caused by inaccurate calibration for the data with SCI (Matsumoto 2007; see `http://www.astro.isas.ac.jp/suzaku/analysis/xis/ver2.0/`)

minology, where the last term represents the reflection component (not including the direct one). In the **pexrav** model, I make the solid angle Ω of the reflector seen from the nucleus as a free parameter, and fix the inclination angle and the cutoff energy at 60° and 300 keV, respectively. The photon index and normalization of the power law are linked to those of the transmitted component. The absorption to the reflection component is set to be independent of that for the transmitted one, by considering a different geometry of the emission region. To check the physical validity of Model B, I examine the equivalent width (E.W.) of the iron-K emission line with respect to the reflection component, E.W.$^{\rm refl}$, obtained from the fit. Theoretically, it is expected to be 1–2 keV (Matt et al. 1991). This value, however, tightly depends on the geometries of the torus and the accretion disk. Thus, I regard the result of Model B as valid only if E.W.$^{\rm refl} = 0.5 - 2$ keV but discard it otherwise.

I finally consider the third model (Model C), where I assume two different absorptions with different covering factors for the transmitted component. This reduces the contribution of a less absorbed reflection component compared with the case of a single absorption as assumed in Model B. In fact, simulations show that the absorber in the torus can be patchy (Wada & Norman 2002), resulting in a time-averaged spectrum that is better modeled by multiple absorptions to the transmitted continuum rather than by a single absorber. In the XSPEC terminology, Model C is expressed as **zphabs*zpcfabs*zhighect*zpowerlw + const*zhighect*zpowerlw + zgauss + zphabs*pexrav**, where the multiple terms of the first component (absorbed, partial covering model) represents the two different absorptions.

To summarize, I can write the three models of the photon spectrum $F(E)$ without the Galactic absorption as follows:

$$\begin{aligned} F(E) = {} & f_{\rm c} \exp\left\{-N_{\rm H}^{\rm a}\sigma(E)\right\} I(E) + (1-f_{\rm c}) \exp\left\{-N_{\rm H}^{\rm b}\sigma(E)\right\} I(E) \\ & + f_{\rm scat} I(E) + G(E) + \exp\left\{-N_{\rm H}^{\rm refl}\sigma(E)\right\} C(E) + S(E), \end{aligned} \tag{2.1}$$

where $f_{\rm c}$ is the fraction of the more heavily absorbed component ($f_{\rm c} = 1$ in Models A and B), $N_{\rm H}^{\rm a}$ and $N_{\rm H}^{\rm b}$ are the absorption column densities for the transmitted component ($N_{\rm H}^{\rm b} = 0$ in Models A and B), $\sigma(E)$ is the cross section of photoelectric absorption, $I(E) \equiv AE^{-\Gamma}\exp\{-E/E_{\rm cut}\}$ is the intrinsic cutoff power law component,

$f_{\rm scat}$ is the scattered fraction, $G\,(E)$ is a gaussian representing the iron-K emission line, $C\,(E)$ is the Compton reflection component ($C\,(E) = 0$ in Model A), and $S\,(E)$ represents additional soft components (see below).

2.3.4 Fitting Results

Using the three models described in the previous subsection, I perform spectral fit simultaneously to the spectra of the FI-XISs (those of 2 or 3 XISs are summed), the BI-XIS, and the HXD/PIN. Based on the fitting results, I chose the best model in the following manner. (1) First, if Models B is found to significantly improve the fit from Model A by performing an F-test, I tentatively adopt Model B as a better model, otherwise Model A. (2) Then, if Model B is found to be physically *not* self-consistent in terms of the E.W. of the iron-K line as explained in the previous subsection, or if Model C significantly improves the fit compared with Model A, I adopt Model C as the best model.

After finding the best one among the three models, I finally include the *Swift*/BAT spectrum to the *Suzaku* data to constrain the photon index most tightly, assuming that the spectral variability is negligible between the observation epoch of *Suzaku* and that of *Swift*. In the fit, I fix the relative normalization between the FI-XISs and the PIN at 1.1 based on the calibration of Crab Nebula (Ishida et al. 2007), while those of the BI-XIS and the BAT against FI-XISs are treated as free parameters, considering the calibration uncertainty and time variability (in flux), respectively. The detailed results of spectral fit for each source is summarized below.

Swift J0138.6–4001

I adopt Model B as the most appropriate model of Swift J0138.6–4001. I obtain $(\chi^2, \nu) = (101.14,\ 96)$ with Model A and $(92.52,\ 94)$ with Model B, where ν is the degree of freedom. Thus, the improvement of the fit by adding a reflection component is found to be significant at >90% confidence level by an F-test, which gives an F-value of 4.38 for the degrees of freedom of $(2,\ 94)$. Since the E.W. of the iron-K line with respect to the reflection component is found to be E.W.$^{\rm refl} > 0.5$ keV, the model

is physically self-consistent. Here I allow the absorption to the reflection component $N_{\rm H}^{\rm refl}$ to be a free parameter, unlike the case in Ueda et al. (2007), where it is linked to that for the transmitted component. The basic results are essentially unchanged, however.

Swift J0255.2–0011

I adopt Model B with a *apec* plasma model for Swift J0255.2–0011. Models A and B yield $(\chi^2,\ \nu) = (596.85,\ 304)$ and $(500.75,\ 302)$, respectively, suggesting the presence of a significant amount of a reflection component. I find E.W.$^{\rm refl} = 0.81^{+0.07}_{-0.09}$ keV with Model B, which is physically consistent. I also confirm that applying Model C does not improve the fit significantly, yielding $f_c = 1.0$ (i.e., multiple absorbers for the transmitted component are not required when we consider a reflection component). As positive residuals remain in the energy band below 1 keV, I add the *apec* model[4] in XSPEC, an emission model from an optically-thin thermal plasma with Solar abundances, over Model B. It greatly improve the fit, giving $(\chi^2, \nu) = (330.38,\ 300)$. The temperature of the plasma is found to be $kT = 0.74^{+0.03}_{-0.10}$ keV with an emission measure of $n^2V \approx 5 \times 10^{63}$ cm^{-3}. This temperature is similar to those found in many Seyfert 2 galaxies (Turner et al. 1997).

Swift J0350.1–5019

Model C is adopted for Swift J0350.1–5019 since I find E.W.$^{\rm refl} < 0.1$ keV . I obtain $(\chi^2, \nu) = (34.93,\ 36)$ with Model A, and $(28.24,\ 35)$ with Model B. Here, I link the absorption to the reflection component and that to the transmitted one, as having the former as a free parameter does not help improving the fit. Model C gives $(\chi^2, \nu) = (28.24,\ 35)$ and E.W.$^{\rm refl} = 2.8^{+1.4}_{-1.3}$ keV, which is now physically consistent.

Swift J0505.7–2348

I adopt Model C with a line feature at ≈0.9 keV as the best description for Swift J0505.7–2348. I find very little reflection component in the spectra of Swift J0505.7–

[4] `http://cxc.harvard.edu/atomdb/`

2348; Models A and B give a very similar χ^2 value of 671.3 for a degree of freedom of 602 and 600, respectively, with no improvement of the fit by Model B. In fact, I obtain a tight upper limit for the reflection component of $R < 0.11$ (90% confidence level) from the fit with Model B. Thus, I apply Model C (here $N_{\rm H}^{\rm refl}$ is tied to $N_{\rm H}^{\rm b}$ since $R \simeq 0$). This model yields $(\chi^2,\ \nu) = (636.11,\ 598)$, which is significantly better than Model A (or B). Furthermore, positive residuals remain in the 0.7–1 keV band, centered at $\simeq$ 0.9 keV. To model this feature, I firstly add an *apec* component to Model C like in the case of Swift J0255.2–0011. This is found to be unsuccessful, largely overestimating the 1–1.2 keV flux of the data. Rather, in some obscured AGNs, emission lines from Ne ions in a photo-ionized plasma are observed around 0.9 keV (e.g., NGC 4507 in Comastri et al. 1998 and NGC 4151 in Ogle et al. 2000), which is a likely origin of the excess feature seen in my spectra. As these emission lines cannot be resolved by CCDs, I model it with a gaussian whose 1σ width is fixed at 0.05 keV, referring to the result of the Seyfert 2 galaxy NGC 4507 (Matt et al. 2004). The center energy of the gaussian is treated as a free parameter, and is found to be 0.87 ± 0.02keV, consistent with my assumption. I obtain $(\chi^2,\ \nu) = (615.08,\ 597)$, which is a significantly better fit compared with Model C without the line.

Swift J0601.9–8636

Model B is adopted for Swift J0601.9–8636. I confirm the results reported in Ueda et al. (2007). Models A and B yield $(\chi^2, \nu) = (45.20,\ 37)$ and $(32.32,\ 35)$, respectively, suggesting a significant amount of a reflection component. As E.W.$^{\rm refl}$ is found to be $2.10^{+0.28}_{-0.30}$ keV, I find Model B to be a physically consistent model for this source.

Swift J1628.1–5145

Model C is adopted for Swift J1628.1–5145. Model A gives $(\chi^2, \nu) = (574.66,\ 546)$, which is significantly improved to $(564.23,\ 544)$ in Model B but with E.W.$^{\rm refl}$ of $<$ 0.1 keV. Hence, I apply Model C to the data, which yields $(\chi^2, \nu) = (553.88,\ 543)$ and a physically consistent value of E.W.$^{\rm refl} = 0.87^{+0.34}_{-0.35}$ keV.

2.3.5 Results Summary

Table 2.4 summarizes the choice of the spectral model (A, B, or C) and best-fit parameters from the *Suzaku* + BAT simultaneous fit for each target. The observed fluxes in the 2–10 keV and 10–50 keV bands and the estimated 2–10 keV intrinsic luminosity corrected for absorption are also listed. I find that all the six targets are heavily obscured with column densities larger than $> 3 \times 10^{23}$ cm^{-2}. As already reported by Ueda et al. (2007), Swift J0601.9–8636 can be called a mildly "Compton thick" AGN, since it shows log $N_{\rm H} > 24$ cm^{-2} but a transmitted component is still seen in the hard X-ray band above 10 keV. I confirm that the photon indices are within the range of 1.6–2.0 for all the targets, and hence the fitting model is physically proper.

The upper panels of Figure 2.3 show the observed spectra of the FI-XIS (black), the BI-XIS (red), and the HXD/PIN (magenta) folded with the detector response in units of counts s^{-1} keV^{-1}, together with the BAT spectra (blue) corrected for the detector area in units of photons cm^{-2} ks^{-1} keV^{-1}. The best-fit models are superposed by solid lines. The lower panels show the residuals in units of χ (i.e., divided by the 1σ statistical error in each bin). Figure 2.4 shows the incident spectra without Galactic absorption in units of EF_E, where the contribution of each component in equation (1) is plotted separately; the black, red, blue, cyan, magenta curves correspond to the total, transmitted component, reflection component, scattered component, and iron-K emission line, respectively. For Swift J0255.2–0011 and Swift J0505.7–2348, the additional soft components are also included in purple and orange, respectively.

For three sources Swift J0138.6–4001, Swift J0255.2–0011, and Swift J0601.9–8636, the best fit reflection strength parameter $R(\equiv \Omega/2\pi) \gtrsim 1$, although values close to unity are allowed within the uncertainties. Most simple geometries only allow $R \approx 1$ to be the maximum physically plausible value. The most likely explanation for these possibly unphysical results is that a part of the direct emission from the nucleus is completely blocked by nonuniform material in the line of sight, reducing the observed normalization of the transmitted component smaller than the true value by a factor of $\lesssim 1/R$ (Ueda et al. 2007). Alternatively, time variability can be responsible

Table 2.4. Best-fit Spectral Parameters

	SWIFT	J0138.6–4001	J0255.2–0011	J0350.1–5019	J0505.7–2348	J0601.9–8636	J1628.1+5145
	Best-fit model	B	B + apec[a]	C	C[b]	B	C
(1)	$N_{\rm H}^{\rm Gal}$ (10^{22} cm^{-2})	0.0163	0.0581	0.0116	0.0212	0.102	0.0183
(2)	$N_{\rm H}$ or $N_{\rm H}^{\rm a}$ (10^{22} cm^{-2})	$65.1^{+4.2}_{-4.6}$	$63.1^{+2.1}_{-1.8}$	85 ± 16	29.3 ± 6.2	115^{+23}_{-18}	58 ± 11
(3)	$N_{\rm H}^{\rm b}$ (10^{22} cm^{-2})	—	—	$8.8^{+3.0}_{-2.1}$	5.868 ± 0.081	—	$12.91^{+0.36}_{-0.45}$
(4)	$f_{\rm c}$	—	—	$0.877^{+0.033}_{-0.037}$	$0.261^{+0.057}_{-0.023}$	—	$0.380^{+0.036}_{-0.039}$
(5)	Γ	$1.755^{+0.081}_{-0.048}$	1.7778 ± 0.022	$1.900^{+0.064}_{-0.070}$	$1.621^{+0.021}_{-0.032}$	$1.962^{+0.066}_{-0.064}$	$1.799^{+0.030}_{-0.029}$
(6)	$f_{\rm scat}$ (%)	$0.276^{+0.070}_{-0.068}$	0.263 ± 0.046	$2.03^{+0.38}_{-0.41}$	$0.857^{+0.067}_{-0.070}$	0.27 ± 0.11	$0.946^{+0.074}_{-0.078}$
(7)	$E_{\rm cen}$ (keV)	$6.375^{+0.026}_{-0.030}$	6.3911 ± 0.0089	$6.40^{+0.20}_{-0.04}$	6.392 ± 0.019	$6.401^{+0.013}_{-0.012}$	$6.275^{+0.067}_{-0.051}$
(8)	E.W. (keV)	0.167 ± 0.042	0.218 ± 0.020	$0.28^{+0.13}_{-0.14}$	$0.062^{+0.012}_{-0.011}$	1.14 ± 0.16	0.051 ± 0.021
(9)	$N_{\rm H}^{\rm refl}$ (10^{22} cm^{-2})	$8.5^{+2.8}_{-2.7}$	$12.4^{+1.9}_{-1.2}$	7.3 (> 0)	($= N_{\rm H}^{\rm b}$)	$3.7^{+3.1}_{-1.4}$	($= N_{\rm H}^{\rm b}$)
(10)	R	$1.00^{+0.36}_{-0.26}$	$1.49^{+0.15}_{-0.23}$	0.28 (< 0.92)	1.4×10^{-7} ($< 9.8 \times 10^{-2}$)	$1.63^{+0.39}_{-0.32}$	$0.43^{+0.22}_{-0.16}$
(11)	F_{2-10} (ergs cm^{-2} s^{-1})	3.4×10^{-12}	4.2×10^{-12}	9.2×10^{-13}	1.1×10^{-11}	1.0×10^{-12}	9.0×10^{-12}
(12)	F_{10-50} (ergs cm^{-2} s^{-1})	3.4×10^{-11}	4.3×10^{-11}	5.5×10^{-12}	2.9×10^{-11}	1.1×10^{-11}	3.6×10^{-11}
(13)	L_{2-10} (ergs s^{-1})	2.4×10^{43}	5.1×10^{43}	1.4×10^{43}	1.5×10^{44}	8.9×10^{41}	1.5×10^{44}
	χ^2/d.o.f.	94.42/97	335.97/307	27.28/39	622.38/604	35.48/38	558.76/550

[a]An additional emission from an optically-thin thermal plasma with Solar abundances is required, modelled by the **apec** code with a temperature of $kT = 0.74^{+0.03}_{-0.10}$ keV and an emission measure of 5×10^{63} cm^{-3} (see text).

[b]An emission line feature at $\simeq 0.9$ keV is required, probably that from Ne ions from a photo-ionized plasma (see text).

Note. — (1) The hydrogen column density of Galactic absorption by Kalberla et al. (2005). (2) The line-of-sight hydrogen column density for the transmitted component. For the double covering model (Model C), that for more heavily absorbed component is given. (3) The smaller line-of-sight hydrogen column density for the transmitted component in Model C. (4) The normalization fraction of the more absorbed component to the total transmitted one in Model C. (5) The power-law photon index. (6) The fraction of the scattered component relative to the intrinsic power law,corrected for the transmission efficiency of $1/R$ if $R > 1$ (see text). (7) The center energy of the iron-K emission line at the rest frame of the source redshift. (8) The observed equivalent width of the iron-K line with respect to the whole continuum. (9) The line-of-sight hydrogen column density for the reflection component. (10) The relative strength of the reflection component to the transmitted one, defined as $R \equiv \Omega/2\pi$, where Ω is the solid angle of the reflector viewed from the nucleus. (11) The observed flux in the 2–10 keV band. (12) The observed flux in the 10–50 keV band. (13) The 2–10 keV intrinsic luminosity corrected for the absorption and the transmission efficiency of $1/R$ if $R > 1$. The errors are 90% confidence limits for a single parameter.

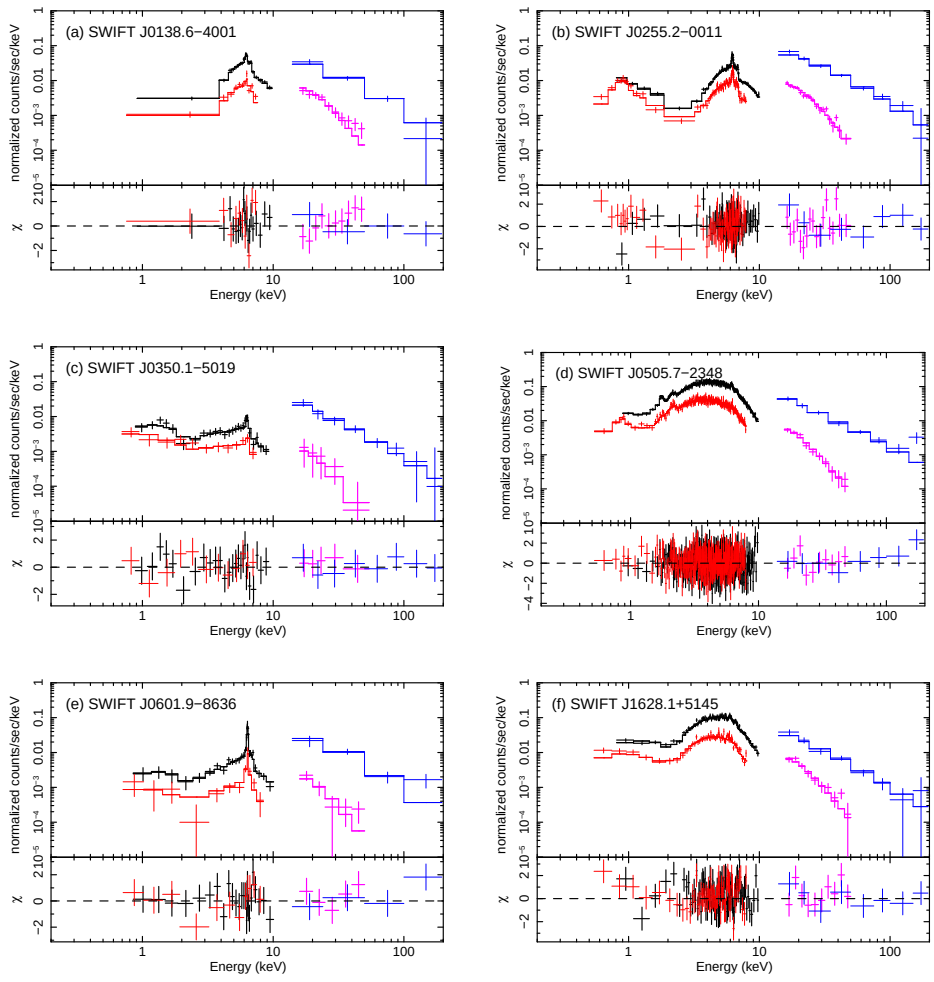

Figure 2.3 The observed spectra of the 6 targets. The black, red, magenta and blue crosses represent the data of the FI-XIS, BI-XIS, HXD/PIN, and BAT, respectively, showing their 1σ errors in vertical direction. The spectra of the XIS and PIN are folded with the detector response in units of counts s^{-1} keV^{-1}, while those of the BAT is corrected for the detector area and have units of photons cm^{-2} ks^{-1} keV^{-1}. The best-fit models are plotted by lines, and the residuals in units of χ are shown in the lower panels.

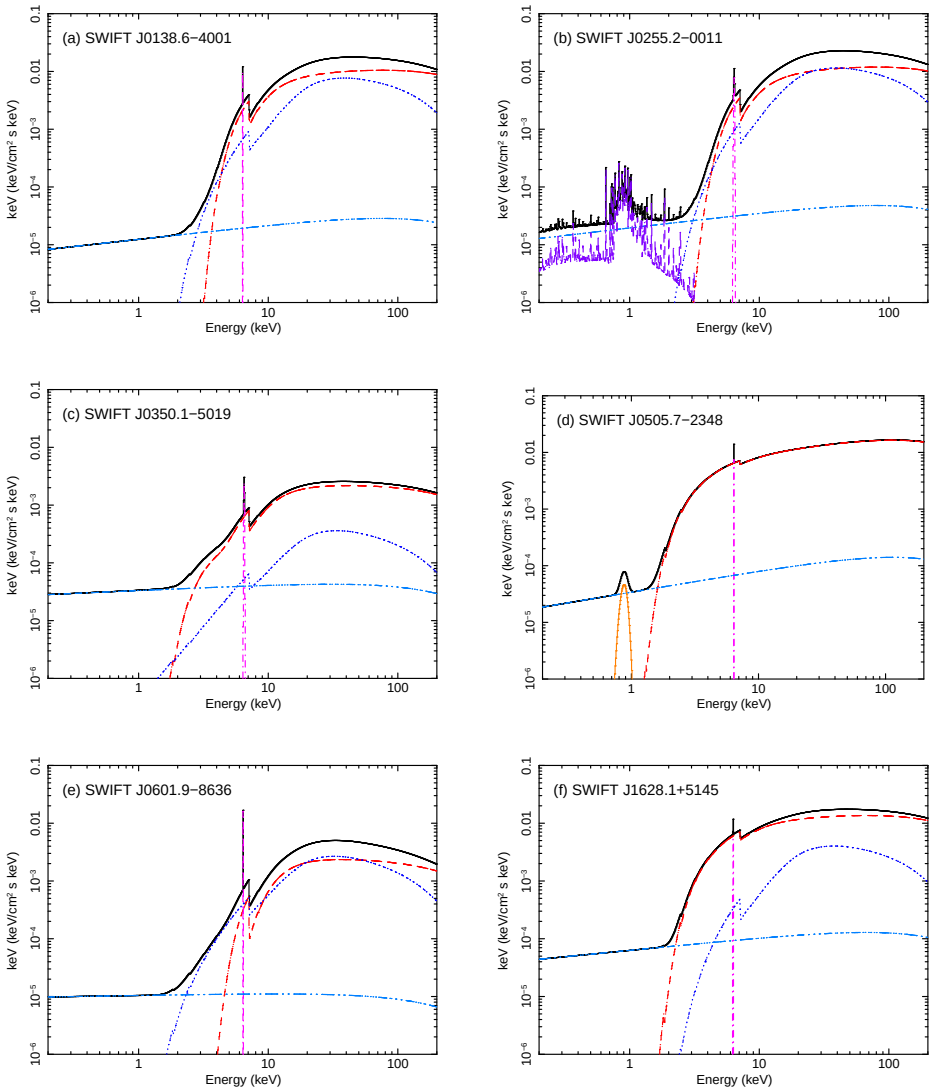

Figure 2.4 The best fit spectral model of the 6 targets in units of EF_E (where E is the energy and F_E is the photon spectrum). The black, dashed red, dotted blue, dot-dot-dashed cyan, dot-dashed magenta curves correspond to the total, transmitted one, reflection component , scattered component, and iron-K emission line, respectively. The purple dashed model in Swift J0255.2–0011 represents the emission from an optically-thin thermal plasma, and the orange one in Swift J0505.7–2348 the Ne emission lines from a photo-ionized plasma (see text).

for this, if we are observing an echo of previously brighter phases of the AGN in the reflection component. Thus, I list in Table 2.4 the intrinsic luminosities corrected for either of these effects by multiplying R. Accordingly, the scattered fraction $f_{\rm scat}$ is corrected by $1/R$ from the observed value, even though this correction does not affect my conclusion.

To evaluate *maximum* possible errors in the spectral parameters due to the uncertainty of the cutoff energy, I also perform fitting by adopting $E_{\rm cut} = 100$ keV instead of 300 keV for Swift J0350.1–5019, Swift J0601.9–8636, and Swift J1628.1–5145, whose 90% lower limits of $E_{\rm cut}$ are smaller than 100 keV as determined with the *Swift*/BAT spectra (§ 2.3.2). I find that Swift J0350.1–5019 shows a smaller scattered fraction ($f_{\rm scat} = 0.77^{+0.58}_{-0.15}$%) compared with the case of $E_{\rm cut}$= 300 keV. For Swift J1628.1–5145, I also obtain a slightly smaller scattered fraction ($f_{\rm scat} = 0.74 \pm 0.06$) with stronger reflection ($R = 0.80^{+0.17}_{-0.23}$) and larger absorption ($N_{\rm H}^{a} = (87 \pm 14) \times 10^{22}{\rm cm}^{-2}$). The other parameters, including those of Swift J0601.9–8636, do not change within the 90% errors. These results indicate that coupling of the spectral parameters with $E_{\rm cut}$ could not always be negligible. Nevertheless, I confirm that it does not affect my discussion below, even considering the largest uncertainties as estimated here.

2.4 Discussion

I have for the first time obtained broad-band spectra covering the 0.5–50 keV band of the six "new" AGNs detected in the *Swift*/BAT survey that did not have precise X-ray observations, including the two sources already reported by Ueda et al. (2007). These six targets were essentially selected without biases, and hence can be regarded as a representative sample of new *Swift*/BAT AGNs. The spectra of all the targets are uniformly described with a spectral model consisting of a heavily absorbed ($\log N_{\rm H} > 23.5$ cm^{-2}) transmitted components with a single or multiple absorptions, scattered lights, a Compton reflection component from optically-thick cold matter, and an iron-K emission line at 6.4 keV in the rest-frame, with additional soft X-ray components in two cases. Thanks to its good sensitivity in the 10–50 keV band and simultaneous band coverage with *Suzaku*, I have accurately derived key spectral

parameters including the fraction of the scattered component $f_{\rm scat}$, the strength of the reflection component $R(=\Omega/2\pi)$, and the E.W. of the iron-K emission line.

The first notable result is that my sample show very small values of $f_{\rm scat}$, $< 3\%$, compared with a typical value of optical selected Seyfert-2 samples of 3–10% (e.g., Turner et al. 1997; Cappi et al. 2006; Guainazzi et al. 2005). Winter et al. (2009) categorize AGNs with $f_{\rm scat} < 3\%$ as "hidden" AGNs, to which all the six sources belong. This is not unexpected, since the "hidden" AGNs constitutes a significant fraction (24%) of the uniform *Swift*/BAT sample.

Figure 2.5 shows the correlation between the reflection strength R versus scattering fraction $f_{\rm scat}$ for my sample. This plot suggests that there are two groups even within the "hidden" population defined by Winter et al. 2009, that is,

- $R \gtrsim 0.8$ and $f_{\rm scat} \lesssim 0.5\%$
- $R \lesssim 0.8$ and $f_{\rm scat} \gtrsim 0.5\%$,

although it is hard to conclude if this distribution is really distinct or continuous, given the small number of the current sample. Following the description by Ueda et al. (2007), I refer to the former group as "new type" and the other "classical type". The new group includes the two sources of Ueda et al. (2007), Swift J0138.6–4001 and Swift J0601.9–8636, and Swift J0255.2–0011. The extremely small scattering fraction indicates two possibilities (1) the opening angle of the torus is small and/or (2) there is very little gas around the torus to scatter the X-rays. Although it is difficult to firmly exclude the latter possibility, the global presence of a reflection component strongly supports the former, as discussed below.

We can constrain the geometry of the torus and viewing angles from the spectral parameters, the scattering fraction, the E.W. of the iron-K line, and absorption column density, based on a simple torus model. Here I utilize the calculation by Levenson et al. (2002), where three free parameters are introduced for a uniform-density torus whose cross-section has a square shape; the thickness of the torus in terms of the optical depth for Thomson scattering τ, the half-opening angle of torus $\theta_{\rm oa}$, and the inclination angle $\theta_{\rm inc}$. In this geometry, the line-of-sight column density of the

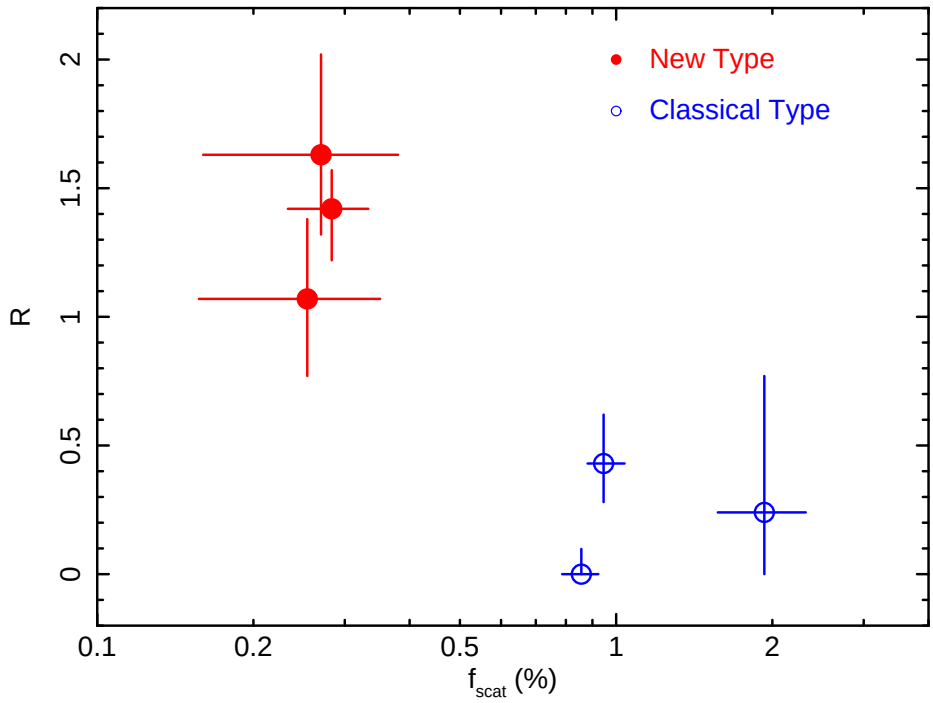

Figure 2.5 The correlation between the strength of the Compton reflection component ($R = \Omega/2\pi$) and the fraction of the scattered component ($f_{\rm scat}$) for the 6 targets. Filled and open circles represent "new type" ($R \gtrsim 0.8$ and $f_{\rm scat} \lesssim 0.5\%$) and "classical type" ($R \lesssim 0.8$ and $f_{\rm scat} \gtrsim 0.5\%$), respectively.

torus depends on $\theta_{\rm inc}$; when we see the nucleus with face-on view, the absorption becomes much smaller than the case of edge-on view. If the column density of the scatterer is constant, the opening angle can be connected to the scattering fraction as

$$\cos\theta_{\rm oa} = 1 - \frac{f_{\rm scat}}{f_{\rm scat,0}}\,(1 - \cos\theta_{\rm oa,0})\,. \tag{2.2}$$

where I normalize $f_{\rm scat} = f_{\rm scat,0}$ at $\theta_{\rm oa} = \theta_{\rm oa,0}$. Assuming $f_{\rm scat,0} = 3\%$ at $\theta_{\rm oa,0} = 45^\circ$ as typical parameters [5], I obtain $\theta_{\rm oa} \sim 20^\circ$ for the new type group. Then, comparing with Figure 2 of Levenson et al. (2002) where $\tau = 4$ is assumed, I can constrain $\theta_{\rm inc} \sim 40^\circ$ for Swift J0601.9–8636, and $\theta_{\rm inc} \sim 20^\circ$ for Swift J0138.6–4001 and Swift J0255.2–0011, from the observed E.W. of the iron-K line (here I have neglected the contribution of an iron-K line originating from the accretion disk, which is often broader than the "narrow" one considered in the spectral model.). The absorption column densities $N_{\rm H} \gtrsim 10^{23.8}$ cm^{-2} and strong reflection $R \gtrsim 1$ are fully consistent with the geometry considered here. The reflection continuum is attributable to that from the inner wall of the tall torus and that from the accretion disk seen with a small inclination angle.

Thus, it is very likely that we are seeing the new type AGNs in a rather face-on geometry through a geometrically and optically thick torus, as discussed in Ueda et al. (2007). An important consequence of this interpretation is that, if we view the same objects in a more edge-on geometry, then these AGNs look heavily Compton-thick ($N_{\rm H} \sim 10^{25}$ cm^{-2}) and hence the transmitted components hardly escape toward us even in the hard X-ray > 10 keV regime due to repeated scattering. Thus, simliar systems to new type AGNs discovered here may still be largely missed even in the on-going *Swift*/BAT or *INTEGRAL* surveys, requiring even more sensitive observations in hard X-rays to detect them more completely.

For the classical type of AGNs, I obtain $\theta_{\rm oa} \gtrsim 30^\circ$ from the observed scattered fraction by equation (2.2). Two sources in this group, Swift J0505.7–2348 and Swift J1628.1–5145, show weak E.W. of the iron-K emission line, ~ 0.05 keV. This is hard to explain by a torus with large τ as assumed in Figure 2 of Levenson et al. (2002), which

[5]The value $\theta_{\rm oa,0} = 45^\circ$ corresponds to the number ratio of obscured AGNs to unobscured ones of about 3, which is consistent with the observations of local AGNs.

predicts E.W. > 0.1 keV if $\theta_{\rm inc} > \theta_{\rm oa}$ (i.e., the transmitted component is absorbed). To consider a torus with different optical depths, I apply a model developed by Ghisellini et al. (1994) (see their Figure 1 for the definition of the geometry). I find that the E.W of the iron-K line and absorption can be consistently explained, within a factor of 2, if the column density of the torus in the equatorial plane is $\sim 10^{23-24}$ cm^{-2} and $60^\circ \leq \theta_{\rm inc} \leq 84^\circ$. The absence of strong reflection components is also consistent with the small optical depth of the torus and with the "edge-on" accretion disk.

To summarize, I have discovered from my first *Swift*-*Suzaku* AGN sample two different classes of obscured AGN population, called "new type" that have an extremely small scattering fraction ($f_{\rm scat} < 0.5\%$) and a strong reflection component ($R \gtrsim 0.8$), and "classical type" with $f_{\rm scat} > 0.5\%$ and $R \lesssim 0.8$. Figure 2.6 shows a schematic illustration of the torus geometry of the two types. It is likely that the new type AGNs are deeply buried in an optically thick torus ($N_{\rm H} \sim 10^{25}$ cm^{-2}) with a small opening angle $\theta_{\rm oa} \sim 20^\circ$, and are viewed in a face-on geometry. By contrast, the classical type AGNs have an optically thin torus ($N_{\rm H} \sim 10^{23-24}$ cm^{-2}) with a larger opening angle $\theta_{\rm oa} \gtrsim 30^\circ$ viewed in a more edge-on geometry than the new type. A significant number of new type AGNs with an edge-on view from us may still be missing in the current all-sky hard X-ray surveys. The presence of two classes of obscured AGNs implies that the understanding of AGN is not as simple as assumed in the population synthesis models of the cosmic X-ray background. Given the small number of my sample, however, it is not clear whether there are two "distinct" types of obscured AGNs or the distribution is continuous. More systematic follow-up observations with *Suzaku* of new *Swift*/BAT AGNs are important to establish the true properties of local AGNs.

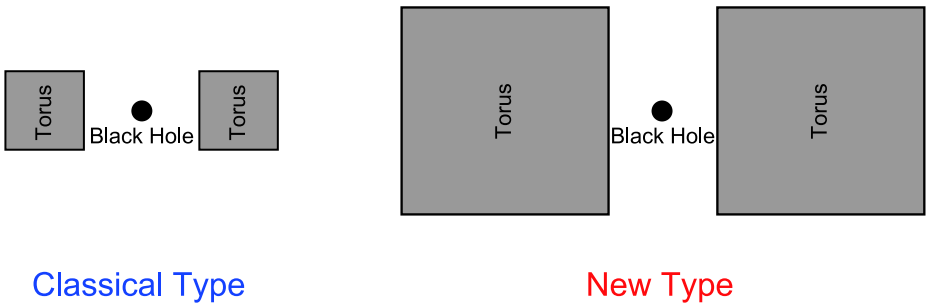

Figure 2.6 The schematic illustration of the torus geometry for the classical type AGNs (left panel) and the new type AGNs (right panel).

Chapter 3

Application of Numerical Torus Models to Two Nearly Compton Thick AGNs (NGC 612 and NGC 3081)

3.1 Introduction

In Chapter 2, I have shown that Type 2 AGNs could be classified into two types, "new type" AGNs with a small scattering fraction and strong reflection strength, and "classical type" ones with a larger scattering fraction and weaker reflection. These types are consistent with SMBHs surrounded by geometrically thick and thin tori, respectively. Using an *INTEGRAL* selected sample, Comastri et al. (2009) also suggest that there are distinct AGN populations of new and classical types, although the result depends on whether the absorption for the reflection component is considered or not in the spectral model (see Comastri et al. 2010). Due to the limited number of objects in the sample studied we are far from reaching a consensus on the torus structure and its dependence on various parameters like the AGN luminosity, Eddington ratio, and properties of the host-galaxy, for the whole AGN populations

In this Chaper, I present the results of detailed X-ray spectral analysis of *Suzaku*

data of NGC 612 and NGC 3081. NGC 612 is a powerful radio galaxy, which was originally classified as Fanaroff-Riley (FR; Fanaroff & Riley 1974) II type by Morganti et al. (1993). This object hosts prominent double radio sources; the eastern lobe has a bright hot spot near its outer edge, while the western one has a jet-like structure. Since the former and latter morphology correspond to those of the FR I and II types, respectively, Gopal-Krishna & Wiita (2000) classifies it as a hybrid morphology radio source. NGC 612 shows an optical spectrum of Seyfert 2 galaxies but the intensity of the [O III] emission is very weak (Parisi et al. 2009). Winter et al. (2008) present the X-ray spectrum observed with *XMM-Newton*, obtaining a large hydrogen column density of $N_{\rm H} \simeq 10^{23.9}$ cm^{-2} with an apparently very flat power-law index of $\simeq$0.3, suggestive of a reflection-dominant spectrum below 10 keV. NGC 3081 is a Seyfert 2 hosted by a barred galaxy. This object has three rings associated with a tidal interaction (Freeman et al. 2000), and exhibits time variable polarization in the optical band (Joshi et al. 1989). The strong [O III] emission is observed from this object (Storchi-Bergmann et al. 1995). Moran et al. (2001) report a large absorption column density ($N_{\rm H} \simeq 10^{23.7}$ cm^{-2}) from the X-ray spectrum observed with *ASCA*.

Section 3.2 describes the observations and data reduction of the two sources. I first analyze the spectra with standard spectral models in Section 3.3, and then present the results of application of the torus model utilizing Monte Carlo calculation by Ikeda et al. (2009) in Section 3.4. The implications of my results are discussed in Section 3.5.

3.2 Observation and Data Reduction

3.2.1 Observation

I observed NGC 612 and NGC 3081 with *Suzaku* in 2008 May and June, respectively. The basic information for my targets is summarized in Table 3.1. *Suzaku* (Mitsuda et al. 2007) carries four X-ray CCD cameras called the X-ray Imaging Spectrometer (XIS-0, XIS-1, XIS-2, and XIS-3) as focal plane imager of four X-ray telescopes, and a non-imaging instrument called the Hard X-ray Detector (HXD)

Table 3.1. List of Targets

SWIFT	Optical/IR Identification	R.A. (J2000)	Dec. (J2000)	Redshift	Classification
J0134.1–3625	NGC 612	01 33 57.74	-36 29 35.7	0.0298	Seyfert 2
J0959.5–2258	NGC 3081	09 59 29.54	-22 49 34.6	0.0080	Seyfert 2

Note. — The position, redshift, and classification for each source is taken from the NASA/IPAC Extragalactic Database.

Table 3.2. Observation Log

Target	Start Time (UT)	End Time	Exposure[a](XIS)	Exposure (HXD/PIN)	SCI[b]
NGC 612	2008 May 20 16:19	May 21 20:08	48.5 ks	41.3 ks	On
NGC 3081	2008 Jun 18 21:49	Jun 19 19:33	43.7 ks	42.4 ks	On

[a]Based on the good time interval for XIS-0.

[b]With/without the spaced-row charge injection for the XIS (Nakajima et al. 2008).

consisting of Si PIN photo-diodes and GSO scintillation counters. XIS-0, XIS-2, and XIS-3 are front-side illuminated CCDs (FI-XISs), while XIS-1 is the back-side illuminated one (BI-XIS). To maximize the effective area of the HXD, the targets were observed at the HXD nominal position, which is about 5 arcmin off-axis from the averaged optical axis of the XISs.[1]

I analyze only the data of the XISs and the HXD/PIN, which covers the energy band of 0.2–12 keV and 10–60 keV, respectively. The fluxes above 50 keV are too faint to be detected with HXD/GSO. Table 3.2 shows the log of the observations. The net exposure of each target is about 45 ks. Because XIS-2 became unoperatable on 2007 November 7 (Dotani et al. 2007), no XIS-2 data are available for both objects. For the XIS observations, I applied spaced-row charge injection (SCI) to improve the energy resolution (Nakajima et al. 2008); for instance, it reduces the full width at half

[1]`http://heasarc.gsfc.nasa.gov/docs/suzaku/analysis/abc/`

maximum of the ^{55}Fe calibration source from $\simeq$ 230 eV to $\simeq$ 160 eV for XIS-0 (Ozawa et al. 2009). To constrain the broad band spectra above 60 keV, I also utilize the *Swift*/BAT spectra covering the 15–200 keV band, integrated over the first 22-months of *Swift* operations.

3.2.2 Data Reduction

The *Suzaku* data are analyzed by using *HEAsoft* version 6.7 and the latest version of *CALDB* on 2009 December 3. For the XIS data, I analyze the version 2.2 cleaned events distributed by the *Suzaku* pipeline processing team. In extraction of the light curves and spectra, I set the source region as a circle around the detected position with a radius of 1.5 arcmin, where about 75% of the total source photons are accumulated, to maximize the signal-to-noise ratio. The background for the XIS data is taken from a source-free region in the field of view with an approximately same offset angle from the optical axis as the source. For the non X-ray background of the HXD/PIN data, I use the so-called "tuned" background model provided by the HXD team. Its systematic errors are estimated to be $\simeq$ 0.97% at a 1σ confidence level in the 15–40 keV band for a 40 ks exposure (Mizuno et al. 2008). Since my exposures are $\approx$ 40 ks or longer, I expect that the error is even smaller than this value. The CXB spectrum simulated with the HXD/PIN response for a uniformly extended emission is added to the non X-ray background spectrum.

3.2.3 Light Curves

Figure 3.1 shows the background-subtracted light curves of my targets obtained with the XIS and HXD/PIN in the 2–10 keV and 15–40 keV bands, respectively. To minimize any systematic uncertainties caused by the orbital change of satellite, I merge data taken during one orbit ($\simeq$ 96 minutes) into one bin. Then, to check if there are any significant time variability during the observations, I perform a simple χ^2 test to each light curve assuming a null hypothesis of a constant flux. The resultant reduced χ^2 value and the degrees of freedom are shown in each panel. As noticed from Figure 3.1, the 2–10 keV flux of NGC 3081 increased by a factor of 1.5 after $\simeq$ 20 ks

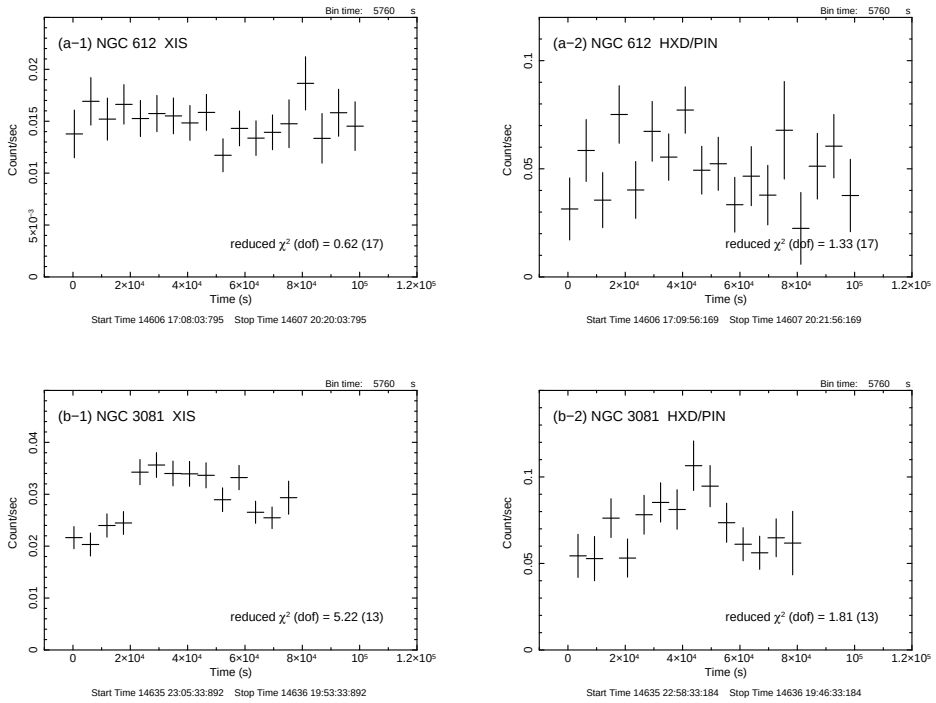

Figure 3.1 The background subtracted light curves of *Suzaku*. One bin corresponds to 96 minutes. The numbers listed in each panel represent the value of reduced χ^2 with the degrees of freedom for the constant flux hypothesis. *Left*: The light curves of the XIS in the 2–10 keV band. The data from the XIS-0 and XIS-3 are summed. *Right*: The light curves of the HXD/PIN in the 15–40 keV band.

Table 3.3. Cutoff Energies ($E_{\rm cut}$) determined by the BAT spectra

$\Omega/2\pi$	NGC 612	NGC 3081
0	> 315	> 338
χ^2/d.o.f.	16.4/6	11.6/6
2	> 319	> 293
χ^2/d.o.f.	10.3/6	5.8/6

Note. — The unit of $E_{\rm cut}$ is keV.

from the start of the observation. Then, a flux decline is suggested between $\simeq$ 50 ks and $\simeq$ 60 ks particularly in the 15–40 keV band. Thus, I divide the observation of NGC 3081 into three different time regions, 0–20 ks (Epoch 1), 20–60 ks (Epoch 2), and 60–80 ks (Epoch 3) measured from the observation start. By contrast, no significant time variability on a time scale of hours are detected from NGC 612. Hence, I analyze the time-averaged spectra over the whole observation for NGC 612.

3.2.4 BAT Spectra

It is known that the incident photon spectra of Seyfert galaxies are roughly approximated by a power law with an exponential cutoff (cutoff power-law model), represented as $AE^{-\Gamma}\exp(-E/E_{\rm cut})$, where A, Γ, $E_{\rm cut}$ are the normalization at 1 keV, photon index, and cutoff energy, respectively. I analyze the *Swift*/BAT spectra in the 15–200 keV band to constrain $E_{\rm cut}$. Here I take into account possible contribution from a Compton reflection component from optically thick, cold matter, utilizing the **pexrav** code Magdziarz & Zdziarski (1995). The relative intensity of the reflection component to that of the intrinsic cutoff power-law component is defined as $R \equiv \Omega/2\pi$, where Ω is the solid angle of the reflector ($R = 1$ corresponds to the reflection from a semi-infinite plane).

In the analysis of the *Swift*/BAT spectra, I assume $R = 0$ or 2 as the two extreme cases just to evaluate the effects of including the reflection components, as done in

Chapter 2. The inclination angle is fixed at 60°. To avoid strong coupling between the power-law slope and cutoff energy, I fix the photon index at 1.9, the canonical slope for AGNs (e.g., Nandra & Pounds 1994). Table 3.3 gives the fitting results for $E_{\rm cut}$; I find that $E_{\rm cut}$ is greater than $\simeq$ 300 keV for both targets.[2] Accordingly, I fix it at 300 keV (or 360 keV for consistency with the Ikeda model) in the following spectral analysis.

3.3 Analytical Models

I perform the spectral fitting to the *Suzaku* data in the same manner as Chapter 2. I start with the simplest model for each target, and if I find that the fit with a simple model does not give a physically self-consistent picture or that the fit is significantly improved by introducing additional parameters, then I adopt more complicated models. I use only the *Suzaku* XIS and HXD/PIN data throughout this stage, and finally perform the simultaneous fit of XIS, HXD/PIN, and *Swift*/BAT spectra with the selected model to obtain the best-fit parameters.

The spectra of FI-XISs are summed, and the relative normalization between the FI-XISs and the PIN is fixed at 1.18 based on the calibration of Crab Nebula (Maeda et al. 2008). Those of BI-XIS and BAT against FI-XISs are set as free parameters. The Galactic absorption ($N_{\rm H}^{\rm Gal}$) is always included in the models, whose hydrogen column density is fixed at values obtained from the H I map Kalberla et al. (2005), available with the **nh** program in the *HEAsoft* package. I adopt the photoelectric absorption cross section by Balucinska-Church & McCammon (1992) ("bcmc"). Different from Chapter 2, I allow the iron abundance to be a free parameter by using **zvphabs** because non Solar values (as defined by Anders & Grevesse 1989) are required to explain the *Suzaku* spectra, while Solar abundances are adopted for the other metals throughout my analysis.

I use the same three models as defined in Chapter 2, consisting of an absorbed transmitted component, a scattered component, and/or an absorbed reflection com-

[2]This conclusion is unchanged when I fix the inclination angle at 30° or 80°, indicating that $E_{\rm cut}$ is not sensitive to the assumed inclination angle.

ponent, with an iron-K emission line:

- Model A: transmission + scattering + iron line,[3]
- Model B: transmission + scattering + iron line + absorbed reflection,[4]
- Model C: transmission with dual absorber + scattering + iron line + absorbed reflection.[5]

In my analysis, I adopt an unabsorbed power law with the same photon index as the incident continuum to describe the scattered component, ignoring any emission lines from the photo-ionized gas. Note that here I only introduce a single absorber for the reflection component as the simplest approximation, although I expect both absorbed and unabsorbed ones from the torus as well as that from the accretion disk, as described in next Section. The **pexrav** component in each spectral model (see footnote) represents only the reflection component not including the direct one by setting $R < 0$, and the inclination angle is fixed at 60°. Theoretically, the equivalent width (E.W.) of the iron-K emission line with respect to the reflection component, E.W.$^{\rm refl}$, is expected to be ∼1 keV (Matt et al. 1991). Since this value depends on the geometry of the reflector as well as the iron abundance, I regard the result as physically valid if E.W.$^{\rm refl}$ = 0.5–2 keV. No other emission lines than iron Kα are significantly detected from the spectra. Considering calibration uncertainties in the energy response of the XISs, I fix the 1σ line width of the iron-Kα emission at the averaged value of the (apparent) line width of the ^{55}Fe calibration source at 5.9 keV: 45 eV and 47 eV for NGC 612 and NGC 3081, respectively.

3.3.1 NGC 612

Model B is adopted as the most appropriate model of NGC 612. I obtain $(\chi^2, \nu) = (90.8, 85)$ with Model A and $(\chi^2, \nu) = (86.9, 84)$ with Model B from the *Suzaku*

[3]In *XSPEC* nomenclature, **zvphabs*zhighect*zpowerlw + const*zhighect*zpowerlw + zgauss**

[4]In *XSPEC* nomenclature, **vzphabs*zhighect*zpowerlw + const*zhighect*powerlw + zgauss + zvphabs*pexrav**

[5]In *XSPEC* nomenclature, **zvphabs*zpcfabs*zhighect*zpowerlw + const*zhighect*zpowerlw + zgauss + zvphabs*pexrav**

spectra, where ν is the degree of freedom. Thus, the improvement of the fit by adding a reflection component is found to be significant at 94% confidence level by an F-test. No significant improvement is found with Model C. For this target, the absorption to the reflection component $N_{\rm H}^{\rm refl}$ is linked to that for the transmitted component, because making them independent does not give a better fit over the statistics (see below). Since the E.W. of the iron-K line with respect to the reflection component is E.W.$^{\rm refl} = 0.7 \pm 0.1$ keV, the model is physically self-consistent; the iron abundance of NGC 612 is roughly half of the Solar value, $0.54^{+0.10}_{-0.07}$, obtained from the simultaneous fit of the *Suzaku* and BAT spectra.

To examine the degeneracy in the fitting parameters, in Figure 3.2 (top) I show the confidence map (in terms of $\Delta\chi^2$) with respect to the strength of the reflection component (R) and its absorption ($N_{\rm H}^{\rm refl}$), based on the Model B fit including the BAT data. Here I do not link $N_{\rm H}^{\rm refl}$ to that of the transmitted component ($N_{\rm H}$), and explore a region of $N_{\rm H}^{\rm refl} < 1.2 \times 10^{24}$ cm^{-2}, the upper limit obtained for $N_{\rm H}$. The contours give the condidence levels at 1σ and 2σ for two interesting parameters. As noticed, while a wide range of $N_{\rm H}^{\rm refl}$ ($\gtrsim 6 \times 10^{23}$ cm$^{-2}, 1\sigma$) is allowed, I can constrain the reflection strength to be $R \simeq 0.6$ for $N_{\rm H}^{\rm refl} < 1.1 \times 10^{24}$ cm^{-2} and $R \simeq 0.3 - 0.7$ otherwise. The case of an unabsorbed reflection component ($N_{\rm H}^{\rm refl} = 0$) or no reflection component ($R = 0$) is rejected at $> 99\%$ confidence level, which corresponds to $\Delta\chi^2 = 9.21$.

3.3.2 NGC 3081

First, I analyze the *Suzaku* spectra integrated over Epoch 1. I obtain $(\chi^2, \nu) = (120.1, 61)$ with Model A and $(\chi^2, \nu) = (80.2, 59)$ with Model B, and thus the improvement of χ^2 is significant at $> 99\%$ confidence level by an F-test. No significant improvement is found with Model C. Finally, since positive residuals remain in the energy band below 1 keV, I add the **vapec**[6] in *XSPEC*, a spectral model from an optically-thin thermal plasma, whose iron abundance is linked to that in the absorber of the transmitted component. This yields a further significantly better fit at $> 99\%$ confidence level with $(\chi^2, \nu) = (50.7, 57)$. The E.W. of the iron-K line with respect to

[6] `http://cxc.harvard.edu/atomdb/`

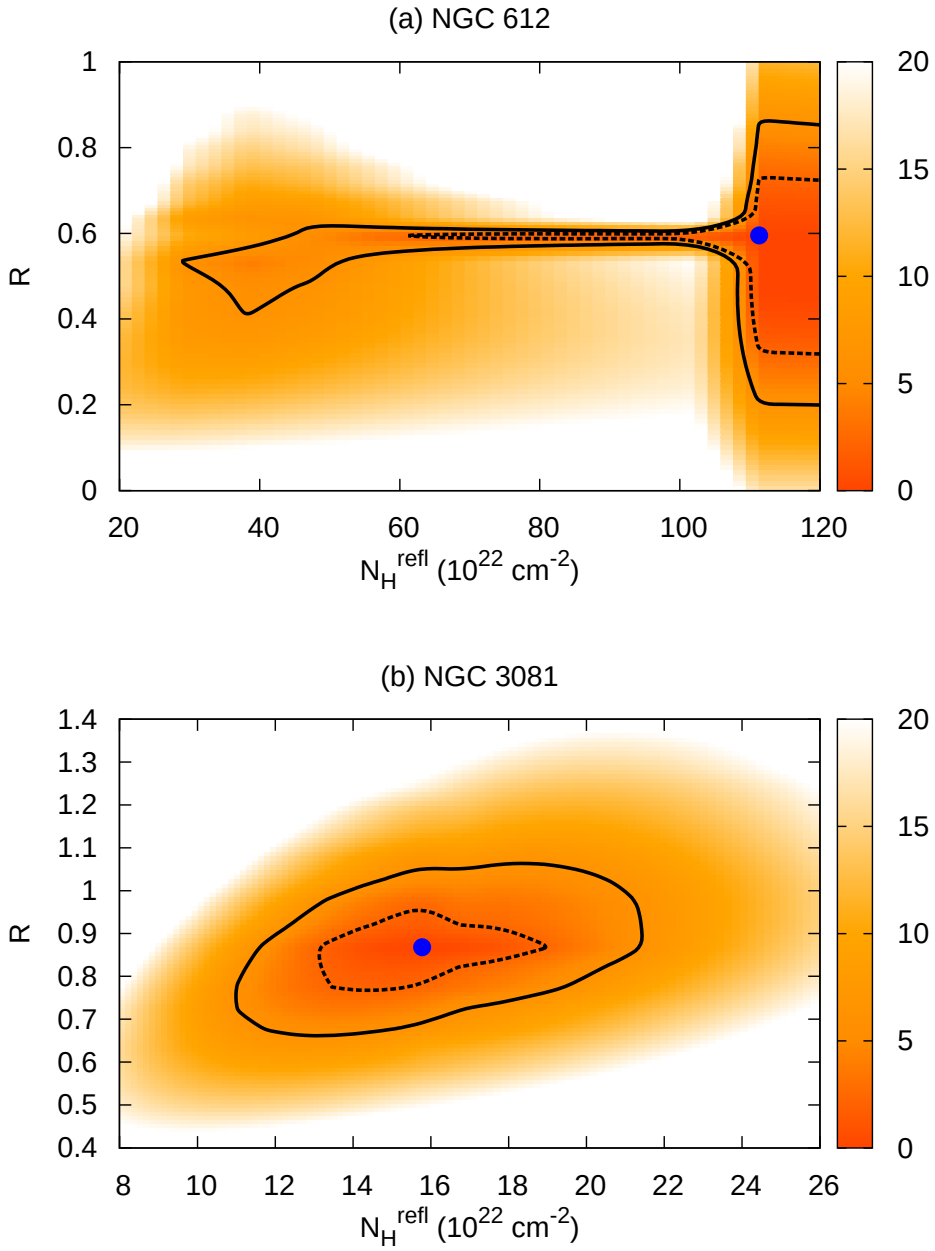

Figure 3.2 The confidence map in $\Delta\chi^2$ (color scale) with respect to the strength of the reflection component ($R = \Omega/2\pi$) and its absorption ($N_{\rm H}^{\rm refl}$) for NGC 612 (top) and NGC 3081 (bottom). The dashed and solid curves correspond to the 1σ and 2σ confidence level for two interesting parameters, respectively.

the reflection component is E.W.$^{\rm refl} = 1.5 \pm 0.3$ keV, which is self-consistent. Thus, I adopt Model B+**vapec** as the best fit model for Epoch 1.

By fitting the Epoch 2 and 3 spectra of *Suzaku* with the same model, I obtain acceptable fits with $(\chi^2, \nu) = (139.7, 114)$ and $(19.1, 30)$, respectively. The best-fit parameters in the three epochs are plotted in Figure 3.3 except for the iron abundance and those of the thin thermal component, which are expected to show no time variability. I find only a weak indication that the column density changed during the observation from $N_{\rm H} = (113 \pm 10) \times 10^{22}$ cm^{-2} (Epoch 1), to $N_{\rm H} = (98 \pm 6) \times 10^{22}$ cm^{-2} (Epoch 2), and then $N_{\rm H} = (86 \pm 10) \times 10^{22}$ cm^{-2} (Epoch 3) in addition to the unabsorbed power-law luminosity, which varied from $L_{2-10} = (3.0 \pm 0.2) \times 10^{42}$ ergs s^{-1} (Epoch 1), to $L_{2-10} = 3.8^{+0.2}_{-0.3} \times 10^{42}$ ergs s^{-1} (Epoch 2), and $L_{2-10} = 2.7^{+0.5}_{-0.2} \times 10^{42}$ ergs s^{-1} (Epoch 3) in the 2–10 keV band. The other parameters are found to be consistent with being constant among the three epochs within the errors. The significance of the variability of the column density is marginal, as the null hypothesis probability of a constant value is found to be 15% from a χ^2 test. Thus, I sum the Epoch 1, 2 and 3 data of *Suzaku* and discuss the time averaged spectra in the following analysis.

To best constrain the spectral parameters of NGC 3081, I perform the simultaneous fit to the time-averaged *Suzaku* and BAT spectra with the Model B+**vapec** model. This yields $(\chi^2, \nu) = 0(199.28, 199)$ and E.W.$^{\rm refl} = 1.0 \pm 0.1$ keV, and thus is physically self-consistent. The iron abundance with respect to Solar is 0.89 ± 0.07, and the temperature of the plasma is found to be $kT = 0.26 \pm 0.02$ keV with an emission measure of $n^2V \simeq 1.5 \times 10^{63}$ cm^{-3}.

Figure 3.2 (bottom) shows the confidence contour map with respect to R and $N_{\rm H}^{\rm refl}$ based on Model B (including the BAT data) for NGC 3081. Unlike the case of NGC 612, the solution is well constrained ($R \simeq 0.8 - 1.0$, 1σ) and we do not see strong degeneracy in the fitting parameters. Again, neither the case of an unabsorbed reflection component ($N_{\rm H}^{\rm refl} = 0$), nor no reflection component ($R = 0$) is allowed at $> 99\%$ confidence level.

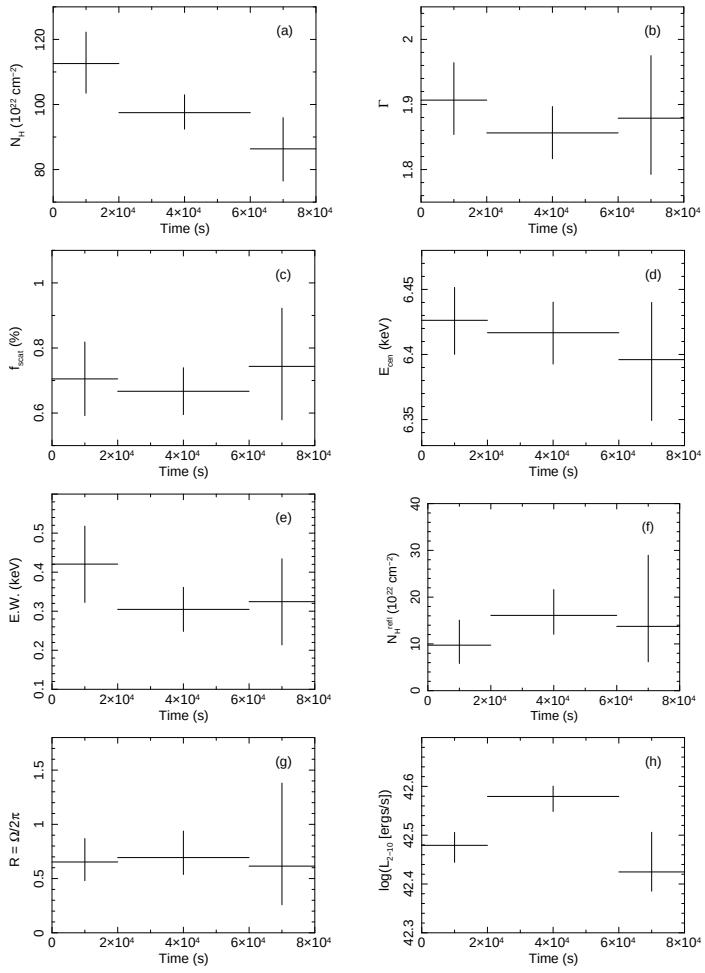

Figure 3.3 Time variability of the best-fit parameters of NGC 3081 obtained with the analytical model: from left to right and top to bottom, (a) the line-of-sight hydrogen column density for the transmitted component, (b) the power-law photon index, (c) the fraction of the scattered component relative to the intrinsic power law, (d) the center energy of the iron-K emission line at the rest frame, (e) the equivalent width of the iron-K line with respect to the whole continuum, (f) the line-of-sight hydrogen column density for the reflection component, (g) the solid angle of the reflection component, (h) the 2–10 keV intrinsic luminosity corrected for the absorption.

3.3.3 Results Summary of Analytical Models

I summarize the best-fit models and parameters in Table 3.4. The observed fluxes in the 2–10 keV and 10–50 keV bands, and the estimated 2–10 keV intrinsic luminosities corrected for absorption are also listed. Figure 3.4 (left) shows the observed spectra of the FI-XIS (black), the BI-XIS (red), and the HXD/PIN (magenta) folded with the detector response in units of counts s^{-1} keV^{-1}, together with the *unfolded* BAT spectra (blue) in units of photons cm^{-2} ks^{-1} keV^{-1}. The best-fit models are superposed by solid lines. In the lower panels, the corresponding data-to-model residuals in units of χ (i.e., normalized by the 1σ statistical error in each bin) are plotted. Figure 3.4 (right) shows the best-fit spectral models in units of EF_E without Galactic absorption, where the contribution of each component is plotted separately; the black, red, blue, cyan, magenta curves correspond to the total, transmitted component, reflection component, scattered component, and iron-K emission line, respectively. For NGC 3081, the additional soft component is also included in purple.

I find that the fraction of the scattered component with respect to the transmitted one for both of NGC 612 and NGC 3081 are fairly small (0.5%–0.8%). Also, they are heavily obscured with column densities of $N_{\rm H} \simeq 10^{24}$ cm^{-2}, and hence can be regarded as nearly "Compton thick" AGNs. Figure 3.5 shows the correlation between the reflection component R and the scattered component $f_{\rm scat}$, superposed on the same plot presented in Chapter 2. NGC 612 and NGC 3081 are located on a similar position to each other in this plot. In Chapter 2, I categorize the observed AGNs into two groups: "new type" with $R \gtrsim 0.8$ and $f_{\rm scat} \lesssim 0.5\%$, and "classical type" with $R \lesssim 0.8$ and $f_{\rm scat} \gtrsim 0.5\%$. Since my targets are placed just between the two types, it is not clear to which "type" these AGNs belong if the intrinsic distribution is indeed distinct. It is also possible that the distribution is smooth and they actually represent an intermediate class bridging the two types.

3.4 Torus Model

Ikeda et al. (2009) performed a set of Monte Carlo simulations to calculate a real-

Table 3.4. Best-fit Spectral Parameters with Analytical Models

		NGC 612	NGC 3081
	Best-fit model	B	B + vapec[a]
(1)	$N_{\rm H}^{\rm Gal}$ (10^{22} cm^{-2})	0.0195	0.0388
(2)	$N_{\rm H}$ (10^{22} cm^{-2})	111 ± 5	98 ± 4
(3)	$Z_{\rm Fe}$	$0.54^{+0.10}_{-0.07}$	0.89 ± 0.07
(4)	Γ	1.90 ± 0.04	1.88 ± 0.02
(5)	$f_{\rm scat}$ (%)	0.55 ± 0.06	0.73 ± 0.07
(6)	$E_{\rm cen}$ (keV)	$6.42^{+0.03}_{-0.02}$	6.41 ± 0.02
(7)	E.W. (keV)	0.28 ± 0.06	0.35 ± 0.05
(8)	E.W.$^{\rm refl}$ (keV)	0.7 ± 0.1	1.0 ± 0.1
(9)	$N_{\rm H}^{\rm refl}$ (10^{22} cm^{-2})	($= N_{\rm H}$)	16^{+4}_{-3}
(10)	R	0.6 ± 0.2	0.9 ± 0.2
(11)	F_{2-10} (ergs cm^{-2} s^{-1})	1.6×10^{-12}	2.7×10^{-12}
(12)	F_{10-50} (ergs cm^{-2} s^{-1})	1.9×10^{-11}	3.1×10^{-11}
(13)	L_{2-10} (ergs s^{-1})	3.0×10^{43}	3.0×10^{42}
	χ^2/d.o.f.	100.4/91	199.3/199

[a]An additional emission from an optically-thin thermal plasma is required, modelled by the **vapec** code with a temperature of $kT = 0.26 \pm 0.02$ keV and an emission measure of 1.5×10^{63} cm^{-3}. The iron abundance is linked to that in the absorber of the transmitted component (see text).

Note. — (1) The hydrogen column density of Galactic absorption by Kalberla et al. (2005). (2) The line-of-sight hydrogen column density for the transmitted component. (3) The iron abundance relative to the Solar value. (4) The power-law photon index. (5) The fraction of the scattered component relative to the intrinsic power law. (6) The center energy of the iron-K emission line at the rest frame of the source redshift. (7) The observed equivalent width of the iron-K line with respect to the whole continuum. (8) The observed equivalent width of the iron-K line with respect to the reflection component (9) The line-of-sight hydrogen column density for the reflection component. (10) The relative strength of the reflection component to the transmitted one, defined as $R \equiv \Omega/2\pi$, where Ω is the solid angle of the reflector viewed from the nucleus. (11) The observed flux in the 2–10 keV band. (12) The observed flux in the 10–50 keV band. (13) The 2–10 keV intrinsic luminosity corrected for the absorption. The errors are 90% confidence limits for a single parameter.

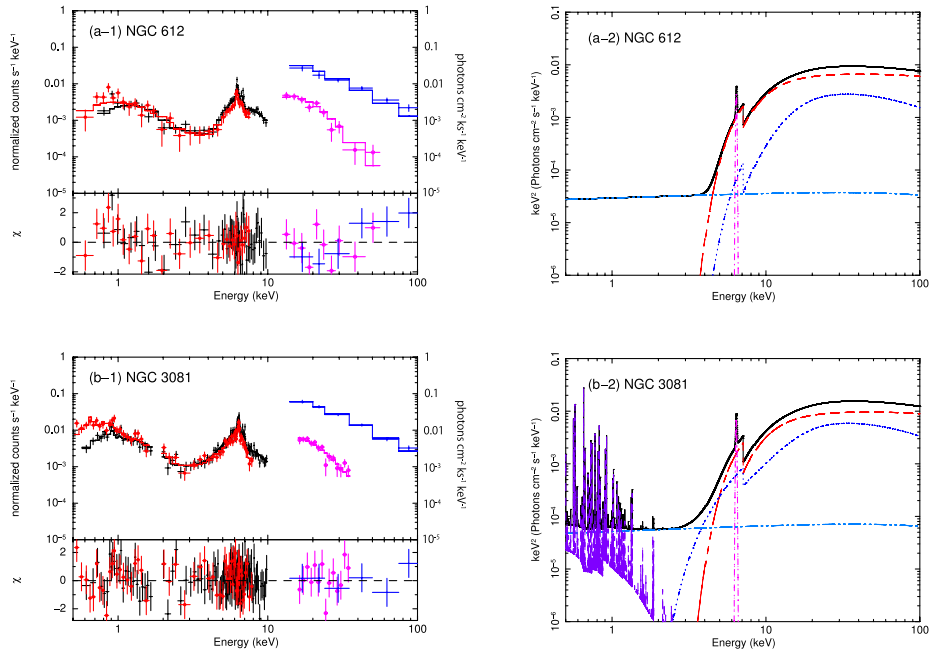

Figure 3.4 The observed spectra (left) and the best-fit spectra model (right) of NGC 612 and NGC 3081. *Left*: The black crosses, red filled circles, magenta open circles, and blue crosses represent the data of the FI-XIS, BI-XIS, HXD/PIN, and BAT, respectively, with 1σ error bars. The spectra of the XIS and PIN are folded with the detector responses in units of counts s^{-1} keV^{-1}, while those of the BAT are *unfolded* spectra in units of photons cm^{-2} ks^{-1} keV^{-1}. The best-fit models are plotted by solid curves, and the residuals in units of χ are shown in the lower panels. *Right*: The best-fit spectral model in units of EF_E (where E is the energy and F_E is the photon spectrum). The black, dashed red, dotted blue, dot-dot-dashed cyan, dot-dashed magenta curves correspond to the total, transmitted one, reflection component, scattered component, and iron-K emission line, respectively. The purple dashed model below 2 keV in NGC 3081 represents the emission from an optically-thin thermal plasma (see text).

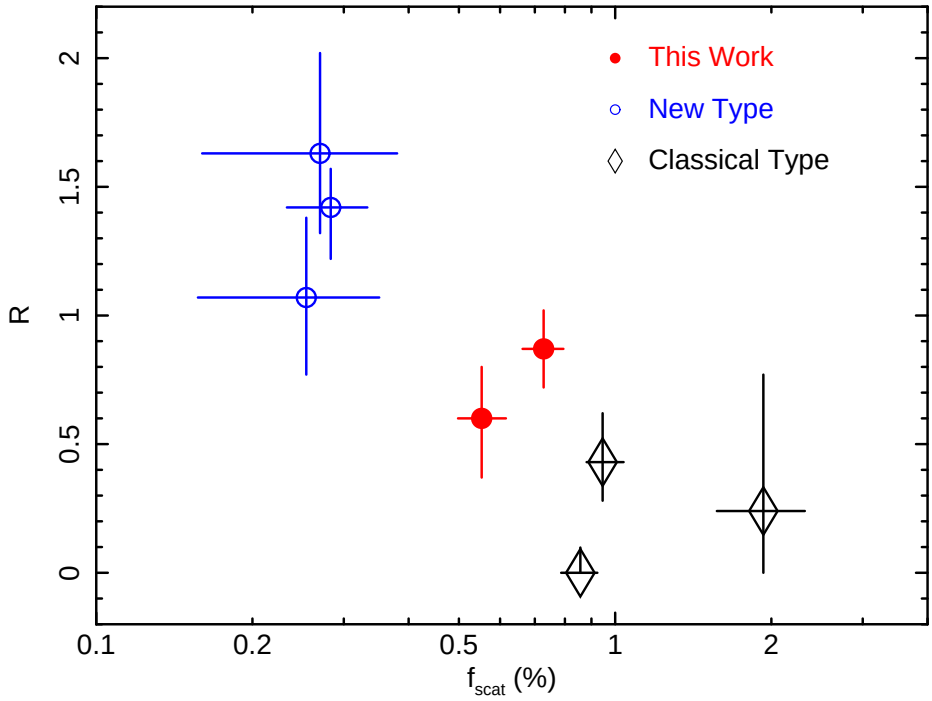

Figure 3.5 The correlation between the strength of the Compton reflection component ($R = \Omega/2\pi$) and the fraction of the scattered component ($f_{\rm scat}$) for my targets (filled circles), superposed on the same figure taken from Figure 2.5, where open circle and open diamond represent "new type" ($R \gtrsim 0.8$ and $f_{\rm scat} \lesssim 0.5\%$) and "classical type" ($R \lesssim 0.8$ and $f_{\rm scat} \gtrsim 0.5\%$) AGNs, respectively.

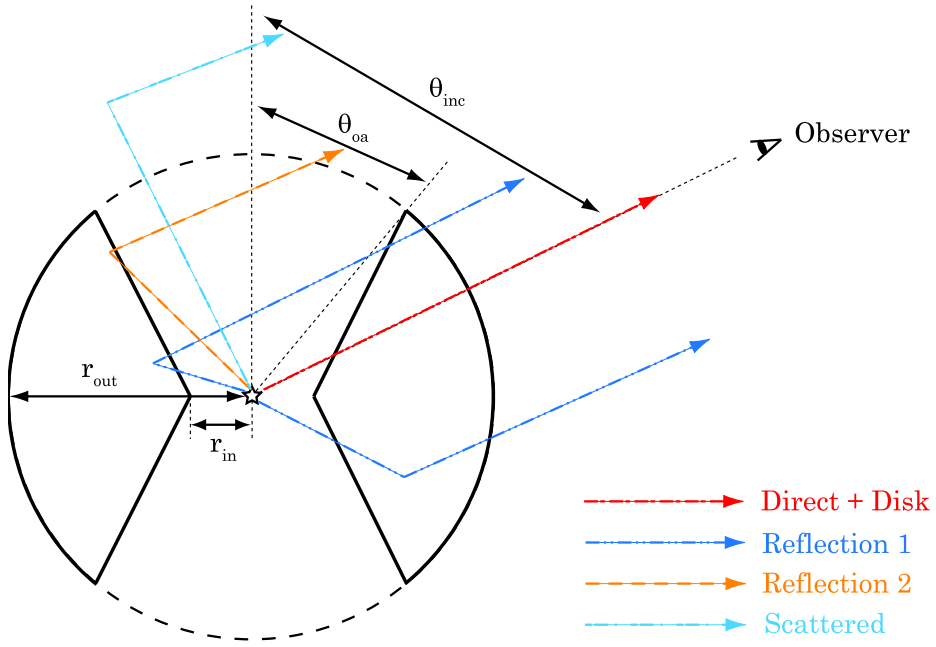

Figure 3.6 Cross-section view of the torus geometry assumed in Ikeda et al. (2009). The torus structure is characterized by the half-opening angle $\theta_{\rm oa}$, the inclination angle of torus from an observer $\theta_{\rm inc}$, the hydrogen column density viewed from the equatorial plane $N_{\rm H}^{\rm Eq}$, and the ratio of $r_{\rm in}$ to $r_{\rm out}$. The observed lights consist of a transmitted component absorbed by the torus (dash-dashed red), a reflection component from the accretion disk absorbed by the torus (dash-dashed red), two reflection components by the torus; "reflection component 1" absorbed by the torus (dash-dot-dotted blue) and "reflection component 2" not absorbed by it (dashed orange). We also consider a scattered component by the surroinding gas, which is not absorbed by the torus (dash-dash-dotted cyan).

istic reprocessed emission from the torus irradiated by a central source, which is assumed to be a cutoff power-law model. In the simulation, they assume a 3-dimensional axis-symmetric uniform torus as illustrated in Figure 3.6. It is characterized by the half-opening angle $\theta_{\rm oa}$, the inclination angle of torus from an observer $\theta_{\rm inc}$, the hydrogen column density viewed from the equatorial plane $N_{\rm H}^{\rm Eq}$, and the ratio r of $r_{\rm in}$ to $r_{\rm out}$.

3.4.1 Method

To perform spectral fitting on XSPEC with the Ikeda et al. (2009) model, I utilize an **atable** model where the resultant spectra from Monte Carlo calculation are stored at grids of the torus parameters in FITS files. Here I refer to the results of the continuum reprocessed from the torus ("torus-reflection component") and those of iron-K fluorescence line, assuming the geometry with $r \equiv r_{\rm in}/r_{\rm out} = 0.01$. The cutoff energy is fixed at $E_{\rm cut} = 360$ keV throughout my analysis, which is consistent with the contraints from the *Swift*/BAT spectra for both targets (> 300 keV). Since the fit is performed only in the 0.5–100 keV range where the table model is available, the choice of $E_{\rm cut}$ hardly affects my results as far as it is higher than $\sim$300 keV. I consider two cases for the elemental abundances; "Solar" abundances (as defined by Anders & Grevesse 1989) and "Subsolar" ones where only those of iron and nickel are set to be 0.5 times Solar values. Finally, the table files have five free parameters; $N_{\rm H}^{\rm Eq}$, $\theta_{\rm oa}$, $\theta_{\rm inc}$, the photon index Γ of the incident continuum, and its normalization at 1 keV.

In the assumed geometry of the torus, the line-of-sight hydrogen column density $N_{\rm H}$ for the transmitted component is related to that along the equatorial plane ($N_{\rm H}^{\rm Eq}$) via equation (3) in Ikeda et al. (2009):

$$\frac{N_{\rm H}}{N_{\rm H}^{\rm Eq}} = \frac{r\left(\cos\theta_{\rm inc} - \cos\theta_{\rm oa}\right) + \sin\left(\theta_{\rm inc} - \theta_{\rm oa}\right)}{(1-r)\left\{r\cos\theta_{\rm inc} + \sin\left(\theta_{\rm inc} - \theta_{\rm oa}\right)\right\}}. \tag{3.1}$$

I introduce **torusabs** (for the fixed Solar abundances) and **vtorusabs** models (for variable abundances) as local models of *XSPEC* to represent photoelectric absorption of the transmitted component, whose line-of-sight column density is related to the torus parameters according to the above equation. In these models I take into

account Compton scattering processes in addition to photoelectric absorption, and hence they can be reliably used even for the Compton thick case. I adopt the photoelectric absorption cross section by Verner et al. (1996) for consistency with Ikeda et al. (2009). As noted by Ikeda et al. (2009), the cross section by Verner et al. (1996) is more accurate for energies above 10 keV than that by Balucinska-Church & McCammon (1992), and is nearly equal to the NIST XCOM database.[7] Since the results become physically meaningless for obscured AGNs if we obtain $\theta_{\rm inc} < \theta_{\rm oa}$, I impose the condition that $\theta_{\rm inc} \geq \theta_{\rm oa} + 1^\circ$ in the fitting process.

The fraction of the scattered component to the transmitted component, $f_{\rm scat}$, should be proportional to the opening solid angle of the torus if the column density of the scattering gas is constant. Thus, I have the constraint that

$$\cos\theta_{\rm oa} = 1 - \frac{f_{\rm scat}}{f_{\rm scat,0}} \left(1 - \cos\theta_{\rm oa,0}\right), \tag{3.2}$$

where I normalize $f_{\rm scat} = f_{\rm scat,0}$ at $\theta_{\rm oa} = \theta_{\rm oa,0} \equiv 45^\circ$. Similarly, I also developed the **fscat** model for *XSPEC* to calculate the normalization of the scattered emission as a function of two parameters, $\theta_{\rm oa}$ and $f_{\rm scat,0}$. Here the normalization parameter $f_{\rm scat,0}$ reflects the averaged column density of the scattering gas and is treated as a free parameter. I allow it to vary within 0.1%–5%; note that a typical value in Seyfert 2 galaxies is $f_{\rm scat} = 3\%$ (Guainazzi et al. 2005).

In addition to the reprocessed emission from the torus, we should also expect a reflection component from the accretion disk in AGN spectra. Thus, in the transmitted component, I include this effect by utilizing the **pexrav** model (Magdziarz & Zdziarski 1995), which is appropriate to represent the reflection component from semi-infinite plane, like that from accretion disks. Here I fix the strength of the disk reflection to be $R \equiv \Omega/2\pi = 1$, where Ω is the solid angle of the accretion disk. The inclination angle of the accretion disk is linked to that of the torus. Although the contribution of this component is not included in the incident photon spectrum in the Ikeda et al. (2009) model, the effects on the "torus reflection" spectra are only second-order and are negligible. For simplicity, hereafter I refer to the total spectrum including the reflection component from the accretion disk as "torus model".

[7] `http://www.nist.gov/pml/data/xcom/index.cfm`

To summarize, I can write the torus model of the photon spectrum $F(E)$ without the Galactic absorption as follows:

$$\begin{aligned} F(E) \quad &= \exp\left\{-N_{\rm H}\left(N_{\rm H}^{\rm Eq}, \theta_{\rm oa}, \theta_{\rm inc}\right)\sigma(E)\right\} I(E) + f_{\rm scat}\left(\theta_{\rm oa}, f_{\rm scat,0}\right) I(E) \\ &+ \exp\left\{-N_{\rm H}\left(N_{\rm H}^{\rm Eq}, \theta_{\rm oa}, \theta_{\rm inc}\right)\sigma(E)\right\} R_{\rm disk}\left(\theta_{\rm inc}, E\right) + R_{\rm refl,1}\left(N_{\rm H}^{\rm Eq}, \theta_{\rm oa}, \theta_{\rm inc}\right) \\ &+ R_{\rm refl,2}\left(N_{\rm H}^{\rm Eq}, \theta_{\rm oa}, \theta_{\rm inc}\right) + \varepsilon_{\rm Fe} L_{\rm Fe}\left(N_{\rm H}^{\rm Eq}, \theta_{\rm oa}, \theta_{\rm inc}\right) + S(E), \end{aligned} \tag{3.3}$$

where $I(E) \equiv AE^{-\Gamma}\exp\left(-E/E_{\rm cut}\right)$ is the intrinsic cutoff power-law component, A is the normalization parameter of the intrinsic cutoff power law at 1 keV, $N_{\rm H}^{\rm Eq}$ is the hydrogen column density of the torus viewed from the equatorial plane, $\theta_{\rm oa}$ is the half-opening angle of the torus, $\theta_{\rm inc}$ is the inclination angle of the torus, $f_{\rm scat,0}$ is the normalization parameter at $\theta_{\rm oa} = 45°$, $N_{\rm H}\left(N_{\rm H}^{\rm Eq}, \theta_{\rm oa}, \theta_{\rm inc}\right)$ is the absorption column density for the transmitted component, $\sigma(E)$ is the cross section of photoelectric absorption, $f_{\rm scat}\left(\theta_{\rm oa}, f_{\rm scat,0}\right)$ is the scattered fraction, $R_{\rm disk}\left(\theta_{\rm inc}, E\right)$ is the Compton reflection component from the accretion disk, $R_{\rm refl,1}\left(N_{\rm H}^{\rm Eq}, \theta_{\rm oa}, \theta_{\rm inc}\right)$ is the torus-reflection component 1 (see Figure 3.6), $R_{\rm refl,2}\left(N_{\rm H}^{\rm Eq}, \theta_{\rm oa}, \theta_{\rm inc}\right)$ is the torus-reflection component 2 (see Figure 3.6), $\varepsilon_{\rm Fe}$ is the normalization parameter for the iron-K emission line, $L_{\rm Fe}\left(N_{\rm H}^{\rm Eq}, \theta_{\rm oa}, \theta_{\rm inc}\right)$ is the iron-K emission line, and $S(E)$ represents additional soft components (for the case of NGC 3081 where the **apec** model is used). I allow the relative normalization of the iron-K line $\varepsilon_{\rm Fe}$ with respect to the torus-reflection components to float between 0.5 and 2, in order to cover the iron abundance range over the fixed values (0.5 or 1.0) and to model the effects of time variability between the transmitted component and the averaged reprocessed emission.

In short, Equation (3.3) is expressed as absorbed transmission[8] + scattering[9] + absorbed accretion disk reflection[10] + absorbed torus reflection[11] + unabsorbed torus reflection[12] + iron line[13]. There are eight free parameters: $\theta_{\rm inc}$, $\theta_{\rm oa}$, $N_{\rm H}^{\rm Eq}$, $f_{\rm scat,0}$, $E_{\rm cen}$, $\varepsilon_{\rm Fe}$, A, and Γ. In the spectral fit, I employ the *MINUIT MIGRAD* method ("migrad")

[8] In *XSPEC* nomenclature, **torusabs*zhighect*zpowerlw**
[9] In *XSPEC* nomenclature, **fscat*zhighect*zpowerlw**
[10] In *XSPEC* nomenclature, **torusabs*toruspexrav**
[11] In *XSPEC* nomenclature, **atable{refl1_torus.fits}**
[12] In *XSPEC* nomenclature, **atable{refl2_torus.fits}**
[13] In *XSPEC* nomenclature, **constant*atable{refl_fe_torus.fits}**

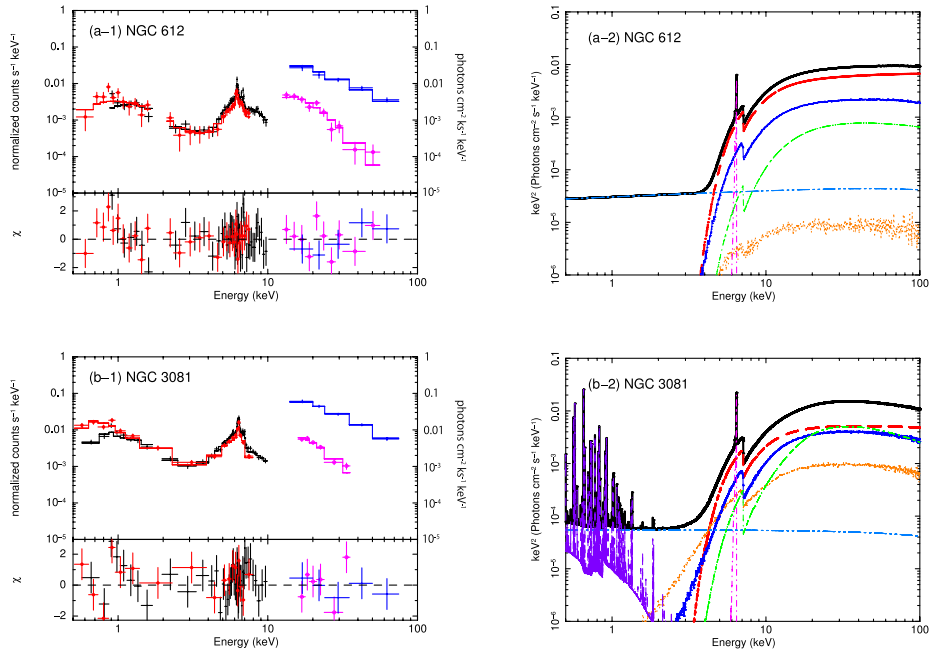

Figure 3.7 The observed spectra (left) and the best-fit spectral model (right) with the torus model. *Left*: same as Figure 3.4 (left). *Right*: the best-fit spectral model in units of EF_E (where E is the energy and F_E is the photon spectrum); total (thick black), transmitted component (thick dashed red), reflection component from the accretion disk (thin dot-dashed green), torus reflection component 1 (thin blue), torus reflection component 2 (thin dotted orange), scattered component (thin dot-dot-dashed cyan), iron-K emission line (thin dot-dashed magenta). The purple dashed curve below 2 keV in NGC 3081 represents the emission from an optically-thin thermal plasma.

as the fitting algorithm, which is found to be more stable than the standard *Levennerg-Marquardt* method ("leven") in my case utilizing the numerical models. Both of the *Suzaku* and BAT spectra (but below 100 keV) are used throughout this section.

3.4.2 Application

NGC 612

Figure 3.7 plots the best-fit torus model, whose parameters are summarized in Table 3.5. The torus model with "Subsolar" abundances is adopted for this target, based

Table 3.5. Best-fit Spectral Parameters with Torus Model

		NGC 612	NGC 3081
(1)	Table model	Subsolar	Solar + apec[a]
(2)	$N_{\rm H}^{\rm Gal}$ (10^{22} cm^{-2})	0.0195	0.0388
(3)	$N_{\rm H}^{\rm Eq}$ (10^{22} cm^{-2})	113^{+10}_{-8}	91^{+10}_{-9}
(4)	$\theta_{\rm oa}$[b](degrees)	70 (>58)	15 ± 2
(5)	$\theta_{\rm inc}$ (degrees)	87 (>76)	19^{+7}_{-1}
(6)	Γ	1.9 ± 0.1	2.0 ± 0.1
(7)	$f_{\rm scat,0}$ (%)	0.14 (<0.19)	4.6 (>3.1)
(8)	$E_{\rm cen}$ (keV)	$6.43^{+0.11}_{-0.02}$	$6.42^{+0.03}_{-0.04}$
(9)	$\varepsilon_{\rm Fe}$	$1.6^{+0.4}_{-0.6}$	0.57 (<0.69)
	χ^2/d.o.f.	84.3/83	209.0/200

[a]An additional emission from an optically-thin thermal plasma with Solar abundances is required, modelled by the **apec** code with a temperature of $kT = 0.25 \pm 0.02$ keV and an emission measure of 1.5×10^{63} cm^{-3} (see text).

[b]The range of the $\theta_{\rm oa}$ is limited to $< 70°$ in the torus model.

Note. — (1) The table model used in the fit. "Solar" means the table with Solar abundances, while "Subsolar" means the table with 0.5-time iron and nickel abundances with respect to Solar ones. (2) The hydrogen column density of Galactic absorption by Kalberla et al. (2005). (3) The hydrogen column density of the torus viewed from the equatorial direction. (4) The half opening angle of the torus. (5) The inclination angle of the torus. (6) The power-law photon index. (7) The fraction of the scattered component relative to the intrinsic power law when the half opening angle of the torus is 45°. (8) The center energy of the iron-K emission line at the rest frame of the source redshift. (9) The relative strength of the iron-K emission line to that predicted by the torus model. The errors are 90% confidence limits for a single parameter.

on the fitting result with the analytical models (Section 3). I find that $\theta_{\rm oa} \simeq 60^\circ - 70^\circ$ and $\theta_{\rm inc} \gtrsim 76^\circ$. As shown in Figure 3.7, the contribution from the reflection component 2 (unabsorbed one) is very small, suggesting that we are seeing the target from an edge-on angle. In such case, the inclination angle $\theta_{\rm inc}$ can be poorly determined above a certain threshold, because the observed line-of-sight hydrogen column density is rather insensitive to $\theta_{\rm inc}$ for a given $N_{\rm H}^{\rm Eq}$ value. Actually, I find that the column density in the equatorial plane, $N_{\rm H}^{\rm Eq} \simeq 10^{24.1}$ cm^{-2}, is close to that along the line of sight ($N_{\rm H}$) as estimated from the analytical model fit. I also find that $f_{\rm scat,0} \simeq 0.14\%$, which indicates that the amount of scattering gas around the nucleus is remarkably small.

NGC 3081

The best-fit parameters with the torus model for NGC 3081 are summarized in Table 3.5 and the model is plotted in Figure 3.7. For this target, I adopt the "Solar" abundance tables based on the analytical model fit. I obtain $\theta_{\rm oa} \simeq 15^\circ$, $\theta_{\rm inc} \simeq 19^\circ$, $N_{\rm H}^{\rm Eq} \simeq 10^{24.0}$ cm^{-2}, and $f_{\rm scat,0} \simeq 4.6\%$. By contrast to NGC 612, $f_{\rm scat,0}$ is rather large, and there is a significant contribution from the unabsorbed reflection component, indicating that the inclination angle must be close to the torus opening angle. The results are consistent with the picture proposed for the "new type" AGN SWIFT J0601.9–8636 (ESO 005–G004) by Ueda et al. (2007), that the nucleus is deeply buried in the geometrically thick torus and is observed from a rather face-on angle.

3.5 Discussion and Conclusion

With *Suzaku* follow-up, I have obtained the best-quality broad band spectra covering the 0.5–60 keV band of two *Swift*/BAT AGNs, NGC 612 and NGC 3081. First, I found a range in the iron abundance; NGC 612 has about 0.5 times Solar abundance of iron (where "Solar" corresponds to Fe/H $= 4.68 \times 10^{-5}$), which is significantly smaller than that of NGC 3081. Applying the analytical models, I find that these objects are nearly Compton thick AGNs with $N_{\rm H} \simeq 10^{24}$ cm^{-2} and the fraction of the scattered

component with respect to the transmitted component is small, $f_{\rm scat} < 0.8\%$, suggesting that these belong to "hidden" population according to Winter et al. (2009). Plotting the results in the $f_{\rm scat}$ versus reflection strength (R) plane, I find these two targets are located just between those occupied by "new type" (geometrically thick tori) and "classical type" AGNs defined in Chapter 2, implying that they would be an intermediate class bridging the two types. We need a larger sample to reveal the true distribution of the whole AGN population in this plane. In this context, simultaneous broad band observations of more "new type" candidates are important to examine their reflection strengths, such as those with small scattering fractions identified from the *XMM-Newton* catalog (Noguchi et al. 2009).

To further investigate the details of the torus geometry of the two AGNs, I apply numerical spectral models based on Monte Carlo simulation where a simple 3-dimensional geometry of the torus is assumed, following the work by Ikeda et al. (2009) and Awaki et al. (2009). I also consider the Compton reflection component from the accretion disk. To my knowledge, this is the first time all effects both from the torus and disk are self-consistently considered in spectral analysis of obscured AGNs. It is remarkable that I am able to reproduce the observed spectra quite well with this torus model, which has only 3 free geometrical parameters; the opening angle, inclination, and equatorial column density.

The column density along the equator plane is found to be $N_{\rm H} \approx 10^{24}$ cm^{-2} for both sources, which is also similar to that found from the Seyfert 2 galaxy Mrk 3 by Ikeda et al. (2009). The relative absence of higher column densities, though very limited in number, may be consistent with the fact that even hard X-rays above 10 keV have a bias against detecting heavily Compton thick AGNs with $N_{\rm H} \sim 10^{25}$ cm^{-2}, unless the sample is limited to the very local universe (Malizia et al. 2009). Thus, a majority of *Swift*/BAT AGNs do not have extremely Compton thick tori defined at the equator plane unless observed from a face-on angle. Future sensitive hard X-ray surveys may start to pick up such populations, whose number density and cosmological evolution are still open questions.

The analysis with the torus model suggest that the torus geometry of the two targets may be different in spite of the very similar results obtained from the analytical

models. My results confirm that the fundamental assumption of the unified model where the opening angles are all the same is too simple. For NGC 612, I find that the opening angle is relatively large ($\simeq 60^\circ - 70^\circ$) and the object is observed from an edge-on angle, consistent with a picture of "classical type" Seyfert 2 galaxies. Similar torus parameters are obtained for Mrk 3 by Ikeda et al. (2009). By contrast, the torus opening angle of NGC 3081 is much smaller ($\simeq 15^\circ$), and we observe it from a face-on angle. This implies that NGC 3081 is closer to a "new type" AGN discovered by Ueda et al. (2007) surrounded by a geometrically thick torus. This picture for NGC 3081 is consistent with the time variability of the column density, because we are seeing the thinnest part of the torus that is expected to be highly patchy (Risaliti et al. 2002). I note, however, that the best-fit torus parameters I obtain from the present analysis should not be taken at their face values, which could depend on the initial assumption of the torus geometry. For instance, as discussed in Ikeda et al. (2009), if I assume a lower value for $r(\equiv r_{\rm in}/r_{\rm out})$ than 0.01, I would obtain a slightly larger half-opening angle $\theta_{\rm oa}$ for the same $N_{\rm H}^{\rm Eq}$ and $\theta_{\rm inc}$ to account for the increased contribution of the unabsorbed reflection component.

Since the observed scattering fraction is similar between the two targets, this difference in the torus opening angle indicates that the amount of scattering gas around the nucleus is much smaller in NGC 621 than in NGC 3081, as represented in the obtained $f_{\rm scat,0}$ value, $f_{\rm scat,0} < 0.2\%$ for NGC 612 and $f_{\rm scat,0} > 3\%$ for NGC 3081. The small amount of the gas in NGC 612 may be consistent with its classification as a "weak emission line" radio galaxy, where the jets expel the surrounding gas. By contrast, the detection of the optically-thin components in NGC 3081 could represent the abundance of the ambient gas around the nucleus.

An important implication from the present study is that the classification of different types of tori (e.g., geometrically thin or thick) based solely on the scattered fraction may be difficult in some cases. My work has demonstrated the power of the application of numerical torus models based on Monte Carlo simulation to best extract the physical view of the nucleus beyond the simple phenomenological spectral analysis, although caution must be paid because I have considered only the simplest geometry by assuming a uniform density. Combinations of the high quality broad

band X-ray spectra with more realistic numerical simulations will be a key approach for further understanding of the nature of AGNs.

Chapter 4

Conclusion

In Chaper 2, I perform the systematic analyses of six *Swift*/BAT AGNs observed with *Suzaku*, and report the results fitted with three analytical models:

- Model A: transmission + scattering + iron line,
- Model B: transmission + scattering + iron line + absorbed reflection,
- Model C: transmission with dual absorber + scattering + iron line + absorbed reflection.

I find that the sources are classified as mildly Compton thick AGNs with the line-of-sight hydrogen column density of $\log N_{\rm H} \gtrsim 23.5$ cm^{-2} except for SWIFT J0505.7–2348. I also find that three of them are fitted well with Model B and obtain very week scattered components ($f_{\rm scat} < 0.3\%$) and strong reflection components ($R \gtrsim 0.8$), while the others are with Model C and obtain rather strong scattered components ($f_{\rm scat} > 0.8\%$) and week reflection components ($R \lesssim 0.8$). As showned in Figure 2.5, there is a negative correlation between R versus $f_{\rm scat}$. This plot also suggets there can be two groups even within obscured AGNs: "new type" ones with $R \gtrsim 0.8$ and $f_{\rm scat} \lesssim 0.5\%$, and "classical type" ones with $R \lesssim 0.8$ and $f_{\rm scat} \gtrsim 0.5\%$. However, the number of my sample is quite limited, and futher investigation is required to confirm this corretion.

Since large E.W. of the iron-K emission line are one of the features of a Compton thick AGN and it gives us useful information for the torus geometry, I compare them

with the numerical simulations by Levenson et al. (2002) and Ghisellini et al. (1994) though different torus geometries are assumed in those papaers; the cross section of the former has a squared shape and that the latter has a spherical shape illustrated as Figure 3.6. The small $f_{\rm scat}$ indicates the small opening angle of the torus if we assumed the uniform density of the scattering gas. I find that we are seeing "new type" sources from a rather face-on geometry ($\theta_{\rm inc} \lesssim 40^{\circ}$) through a geometrically and optically thick torus, while that we are seeing "classical type" sources from an edge-on geometry ($\gtrsim 60^{\circ}$). Note that these pictures are obtained by assuming different torus geometries. For further correct understanding, we require consecutive spectral templates which can describe those of Compton thick AGNs.

In Chapter 3, I report the results of two nearly Compton thick AGNs (NGC 612 and NGC 3081) obtained with *Suzaku*. The same models applied to six AGNs in Chaper 2 (or described above) yield $R = 0.4-1$ and $f_{\rm scat} = 0.5-0.8\%$, this indicating that the torus geometries of these two objects are very similar, while the [O III]λ5007 fluxies of both sources convice us that NGC 612 could be a "new type" AGN and NGC 3081 could be a "classical type" one. To obtain futher information for the tori, I apply the results of Monte Carlo simulations performed by Ikeda et al. (2009), which is the one I have missed in Chaper 2 and enables us to compare the torus geometries of "new type" and "classical types" directly. I unexpectedly find that NGC 612 has a "classical type" torus, and that the weak scattered component and [O III] emission are caused by the very small fraction of the scattering gas, while that NGC 3081 has a "new type" torus, and that we are seeing this object from a face-on angle. In addition, these pictures are consistent with the morphorogy in the radio band (NGC 612) and the optical band (NGC 3081). My study demostrates that combinations of the high quality broad band X-ray spectra with more realistic numerical simulations will be a key approach for further understanding of the nature of AGNs.

Ikeda et al. (2009) assumes only one torus geometry; Murphy & Yaqoob (2009) studies the reflection from a torus in a doughnut-like shape as MYTORUS, which is often illustrate in a cartoon describing the unified model of AGNs. Since the opening angle of the torus is fixed at 60° in the MYTORUS model, it does not match the aims of my studies. However, the authors of MYTORUS promise us that the future

version allows us to change the opening angles on their website.[1] We can obtain the torus parameters with different geometries and can investigate deeply the nature of AGNs if it is available. I believe that my studies described in this Ph.D. thesis are a milestone for future.

[1] http://www.mytorus.com/

Bibliography

Anders, E., & Grevesse, N. 1989, Geochim. Cosmochim. Acta, 53, 197

Antonucci, R. R. J., & Miller, J. S. 1985, ApJ, 297, 621

Awaki, H., Terashima, Y., Higaki, Y., & Fukazawa, Y. 2009, PASJ, 61, 317

Balucinska-Church, M. & McCammon, D. 1992, ApJ, 400, 699

Bassani, L., et al. 2006, ApJ, 636, L65

Cappi, M., et al. 2006, A&A, 446, 459

Comastri, A., Vignali, C., Cappi, M., Matt, G., Audano, R., Awaki, H., & Ueno, S. 1998, MNRAS, 295, 443

Comastri, A., Iwasawa, K., Gilli, R., Vignali, C., & Ranalli, P. 2009, arXiv:0910.1025

Comastri, A., Iwasawa, K., Gilli, R., Vignali, C., Ranalli, P., Matt, G., & Fiore, F. 2010, ApJ, 717, 787

Dotani, T. & the XIS team 2007, JX-ISAS-SUZAKU-MEMO-2007-08

Eguchi, S., Ueda, Y., Terashima, Y., Mushotzky, R., & Tueller, J. 2009, ApJ, 696, 1657

Fanaroff, B. L., & Riley, J. M. 1974, MNRAS, 167, 31P

Freeman, T., Byrd, G., & Ousley, D. 2000, IAU Colloq. 174: Small Galaxy Groups, 209, 325

Ghisellini, G., Haardt, F., & Matt, G. 1994, MNRAS, 267, 743

Giacconi, R., Gursky, H., Paolini, F. R., & Rossi, B. B. 1962, Physical Review Letters, 9, 439

Gilli, R., Comastri, A., & Hasinger, G. 2007, A&A, 463, 79

Gopal-Krishna, & Wiita, P. J. 2000, A&A, 363, 507

Guainazzi, M., Matt, G., & Perola, G. C. 2005, A&A, 444, 119

Hasinger, G., Burg, R., Giacconi, R., Hartner, G., Schmidt, M., Trumper, J., & Zamorani, G. 1993, A&A, 275, 1

Hasinger, G., Burg, R., Giacconi, R., Schmidt, M., Trumper, J., & Zamorani, G. 1998, A&A, 329, 482

Hasinger, G. 2008, A&A, 490, 905

Hickox, R. C., & Markevitch, M. 2006, ApJ, 645, 95

Hopkins, P. F., Hernquist, L., Cox, T. J., Di Matteo, T., Martini, P., Robertson, B., & Springel, V. 2005, ApJ, 630, 705

Hopkins, P. F., Hernquist, L., Cox, T. J., Di Matteo, T., Robertson, B., & Springel, V. 2006, ApJS, 163, 1

Ikeda, S., Awaki, H., & Terashima, Y. 2009, ApJ, 692, 608

Ishida, M., Suzuki, K., & Someya, K., 2007, JX-ISAS-SUZAKU-MEMO-2007-11

Joshi, U. C., Jain, R., & Deshpande, M. R. 1989, Active Galactic Nuclei, 134, 321

Kalberla, P. M. W., Burton, W. B., Hartmann, D., Arnal, E. M., Bajaja, E., Morras, R., Pöppel, W. G. L. 2005, A&A, 440, 775

Koyama, K., et al. 2007, PASJ, 59, 23

Krivonos, R., Revnivtsev, M., Lutovinov, A., Sazonov, S., Churazov, E., & Sunyaev, R. 2007, A&A, 475, 775

Levenson, N. A., Krolik, J. H., Życki, P. T., Heckman, T. M., Weaver, K. A., Awaki, H., & Terashima, Y. 2002, ApJ, 573, L81

Maeda, Y., Someya, K., Ishida, M., & the XRT team, Hayashida, K., Mori, H., & the XIS team 2008, JX-ISAS-SUZAKU-MEMO-2008-06

Magdziarz, P., & Zdziarski, A. A. 1995, MNRAS, 273, 837

Magorrian, J., et al. 1998, AJ, 115, 2285

Maiolino, R., et al. 2003, MNRAS, 344, L59

Malizia, A., Stephen, J. B., Bassani, L., Bird, A. J., Panessa, F., & Ubertini, P. 2009, MNRAS, 399, 944

Marconi, A., & Hunt, L. K. 2003, ApJ, 589, L21

Matsumoto, H. & the XIS team, 2007, JX-ISAS-SUZAKU-MEMO-2007-06

Matt, G., Perola, G. C., & Piro, L. 1991, A&A, 247, 25

Matt, G., Bianchi, S., D'Ammando, F., & Martocchia, A. 2004, A&A, 421, 473

McHardy, I. M., et al. 1998, MNRAS, 295, 641

Mitsuda, K., et al. 2007, PASJ, 59, 1

Mizuno, T., et al. 2008, JX-ISAS-SUZAKU-MEMO-2008-03

Moran, E. C., Kay, L. E., Davis, M., Filippenko, A. V., & Barth, A. J. 2001, ApJ, 556, L75

Morganti, R., Killeen, N. E. B., & Tadhunter, C. N. 1993, MNRAS, 263, 1023

Murphy, K. D., & Yaqoob, T. 2009, MNRAS, 397, 1549

Nakajima, H., et al. 2008, PASJ, 60, 1

Nandra, K., & Pounds, K. A. 1994, MNRAS, 268, 405

Noguchi, K., Terashima, Y., & Awaki, H. 2009, ApJ, 705, 454

Ogle, P. M., Marshall, H. L., Lee, J. C., & Canizares, C. R. 2000, ApJ, 545, L81

Ozawa, M., et al. 2009, PASJ, 61, 1

Parisi, P., et al. 2009, A&A, 507, 1345

Risaliti, G., Elvis, M., & Nicastro, F. 2002, ApJ, 571, 234

Sako, M., Kahn, S. M., Paerels, F., & Liedahl, D. A. 2000, ApJ, 543, L115

Storchi-Bergmann, T., Kinney, A. L., & Challis, P. 1995, ApJS, 98, 103

Takahashi, T., et al. 2007, PASJ, 59, 35

Tueller, J., Mushotzky, R. F., Barthelmy, S., Cannizzo, J. K., Gehrels, N., Markwardt, C. B., Skinner, G. K., & Winter, L. M. 2008, ApJ, 681, 113

Turner, T. J., George, I. M., Nandra, K., & Mushotzky, R. F. 1997, ApJS, 113, 23

Ueda, Y., Akiyama, M., Ohta, K., & Miyaji, T. 2003, ApJ, 598, 886

Ueda, Y., et al. 2007, ApJ, 664, L79

Urry, C. M., & Padovani, P. 1995, PASP, 107, 803

Verner, D. A., Ferland, G. J., Korista, K. T., & Yakovlev, D. G. 1996, ApJ, 465, 487

Wada, K., & Norman, C. A. 2002, ApJ, 566, L21

Winter, L. M., Mushotzky, R. F., Tueller, J., & Markwardt, C. 2008, ApJ, 674, 686

Winter, L. M., Mushotzky, R. F., Reynolds, C. S., & Tueller, J. 2009, ApJ, 690, 1322

Appendix A

Application of Numerical Torus Models to Swift J0255.2–0011 and Swift J0505.7–2348

In Chapter 3, I apply the numerical torus model by Ikeda et al. (2009) to not sources described in Chaper 2, but other new sources. It is curious that I confirm whether the same results are reproduced with the torus model. However, the torus model could give us multiple solutions if the quality of data is not good. In this chapter, I briefly report the results with the torus model for Swift J0255.2–0011 (new type) and Swift J0505.7–2348 (classical type), whose exposures are longest in the six sources.

The spectral model is described as Equation 3.3. As found in Chapter 2, the relative strength of the reflection component to the transmitted one is hardly detected for Swift J0505.7–2348 ($R < 0.1$). Hence fixing the strength of the disk reflection to be $R_{\rm disk} \equiv \Omega/2\pi = 1$, where Ω is the solid angle of the accretion disk, causes an unacceptable fitting result. Here I treat $R_{\rm disk}$ as a free parameter for this source, while I fix that for Swift J0255.2–0011 at $R_{\rm disk} = 1$.

I summarize the best-fit parameters in Table A.1. For Swift J0255.2–0011, I obtain $N_{\rm H}^{\rm Eq} = 10^{23.9}$ cm^{-2}, $\theta_{\rm oa} \simeq 16°$, and $\theta_{\rm inc} \simeq 17°$, this meaning that this object has a new-type torus and we are seeing this object from a rather face-on angle. This

Table A.1. Best-fit Spectral Parameters with Torus Model

	SWIFT	J0255.2–0011	J0505.7–2348
(1)	Table model	Solar + apec[a]	Solar + line[b]
(2)	$N_{\rm H}^{\rm Gal}$ (10^{22} cm^{-2})	0.0581	0.0212
(3)	$N_{\rm H}^{\rm Eq}$ (10^{22} cm^{-2})	80 ± 2	$8.2^{+0.2}_{-0.1}$
(4)	$\theta_{\rm oa}$ (degrees)	$16.0^{+0.3}_{-0.9}$	47^{+5}_{-11}
(5)	$\theta_{\rm inc}$ (degrees)	$17.1^{+0.3}_{-0.9}$	48^{+12}_{-5}
(6)	Γ	1.80 ± 0.02	1.50 (< 1.52)
(7)	$R_{\rm disk}$	1[c]	3.7×10^{-2} (< 0.15)
(8)	$f_{\rm scat,0}$ (%)	$1.4^{+0.3}_{-0.4}$	1.06 (< 1.14)
(9)	$E_{\rm cen}$ (keV)	$6.42^{+0.02}_{-0.03}$	$6.39^{+0.02}_{-0.09}$
(10)	$\varepsilon_{\rm Fe}$	0.57 ± 0.06	1.4 ± 0.2
	χ^2/d.o.f.	415.0/359	638.2/593

[a]An additional emission from an optically-thin thermal plasma with Solar abundances is required, modelled by the **apec** code with a temperature of $kT = 0.64 \pm 0.05$ keV and an emission measure of 5×10^{63} cm^{-3}.

[b]n emission line feature at $\simeq 0.9$ keV is required, probably that from Ne ions from a photo-ionized plasma.

[c]Fixed.

Note. — (1) The table model used in the fit. "Solar" means the table with Solar abundances, while "Subsolar" means the table with 0.5-time iron and nickel abundances with respect to Solar ones. (2) The hydrogen column density of Galactic absorption by Kalberla et al. (2005). (3) The hydrogen column density of the torus viewed from the equatorial direction. (4) The half opening angle of the torus. (5) The inclination angle of the torus. (6) The power-law photon index. (7) The relative strength of the reflection component to the transmitted one, defined as $R_{\rm disk} \equiv \Omega/2\pi$, where Ω is the solid angle of the reflector viewed from the nucleus. (8) The fraction of the scattered component relative to the intrinsic power law when the half opening angle of the torus is 45°. (9) The center energy of the iron-K emission line at the rest frame of the source redshift. (10) The relative strength of the iron-K emission line to that predicted by the torus model. The errors are 90% confidence limits for a single parameter.

picture is consistent with the discussion utilizing the E.W. of the iron emission line in Chapter 2. For Swift J0505.7–2348, I obtain $N_{\rm H}^{\rm Eq} = 10^{22.9}$ cm^{-2}, $\theta_{\rm oa} \sim 47^{\circ}$, and $\theta_{\rm inc} \sim 48^{\circ}$. These results are also consistent with the discussion in Chapter 2, except for the inclination angle.

These results give us an important conclusion; if the fraction of the scattering gas around a torus can be assumed as same, the E.W. of the iron emission line provides rather accurate information about the torus geometry. Hence the method utilizing the E.W. of the iron line is still a powerful tool even when an observed X-ray spectrum does not have enough quality to apply our torus model if we can estimate the fraction of the scattering gas in other wavelengths.